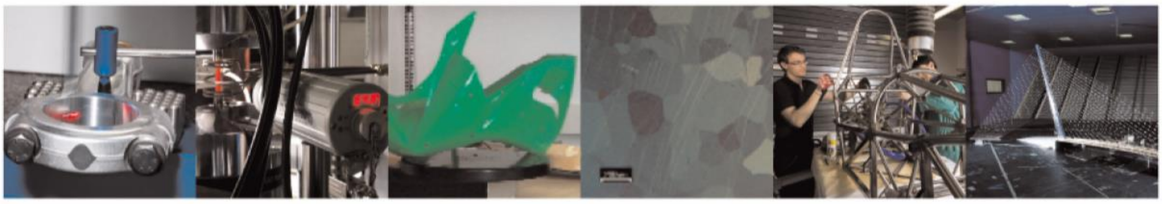

Feasibility Study Of A Multi-Parameter Probability Of Detection Formulation For A Lamb Waves-Based Structural Health Monitoring Approach To Light Alloy Aeronautical Plates

Andrea Gianneo, Michele Carboni and Marco Giglio

This is a post-peer-review, accepted for publication, pre-copyedit version of an article published in Structural Health Monitoring. The final authenticated version is available online at: http://dx.doi.org/10.1177/1475921716670841

Feasibility Study of a Multi-Parameter Probability of Detection formulation for a Lamb Waves Based Structural Health Monitoring Approach to Light Alloy Aeronautical Plates

A. Gianneo, M. Carboni[1], M. Giglio

Department of Mechanical Engineering, Politecnico di Milano, Via La Masa 1, 20156 Milano, Italy

Abstract

In view of an extensive literature about guided waves based structural health monitoring of plate-like structures made of metallic and composite materials, a lack of information is pointed out regarding an effective and universally accepted approach for characterizing capability and reliability in detecting, localizing and sizing in-service damages. On the other hand, in the frame of traditional non-destructive testing systems, capability is typically expressed by means of suitable "Probability of Detection" curves based on

---

[1] Corresponding author: Tel.: +39-02-23998253, Fax: +39-02-23998202, E-mail: michele.carboni@polimi.it

Berens' model, where a linear relationship is established between probability of detection and flaw size. Although the uncertain factors are usually different between a non-destructive inspection technique and a structural health monitoring approach, it seems a similar mathematical framework could be assumed. From this point of view, the present research investigates the feasibility of application of the very recent "Multi-Parameter" Probability of Detection approach, developed within the traditional non-destructive testing field, to guided waves based structural health-monitoring. In particular, numerical simulations as well as experimental responses from flawed aluminium alloy plates were combined to bring about a "Master" Probability of Detection curve. Once established, this curve can be used to study the intrinsic capability of the system in terms of Probability of Detection curves, overcoming the intrinsic limitation of a single predictor (like the crack size) and a statistical model typically based upon a linear behaviour between the predictor and the response.

Keywords

Lamb Waves, Structural Health Monitoring, Probability of Detection, Finite Element Method, Aluminium Alloy

Introduction

In spite of the high level of reliability nowadays reached by non-destructive testing (NDT) techniques, maintenance and repairs of safety components and systems represent a considerable amount of operational costs; moreover, a significant amount of civil, aeronautical, power generation and military structures has, today, exceeded its design lifetime [1]. Therefore, an increasing solution, proposed in the literature [2], is the application of Structural Health Monitoring (SHM) approaches which, in the aeronautical field, have shown the potentiality to significantly decrease [1] the overall costs of traditional NDT, since planned in-service interruptions can be substituted by condition-based maintenance. More importantly, SHM can prevent catastrophic disasters by identifying and monitoring developing defects before their degeneration into a failure, with significant improvements in reliability. Nowadays, the applied SHM techniques are, in general, based onto different physical phenomena [2,3]: dynamic modal data, electro-mechanical impedance, static parameters (displacement field, strain gauges, optical fibres, etc.), acoustic emission (AE) and elastic waves. Those capitalizing on modal data are generally [3,4] less sensitive to damage until it reaches a threshold value able to influence the global dynamic response of the material/component, whereas electro-mechanical impedance and static parameters are relatively insensible [3,5,6] to damage developing far away from the transducers. AE is generated by developing damages in terms of elastic waves and it is an effective way of localization via triangulation and of evaluation of the failure behaviour [7]. However, it is a passive technique, so it requires loaded components and it is prone to environmental noise contamination. Furthermore, most of the aforementioned techniques employ bulky transducers (AE), require point scanning [3,8,9] (strain gauges, optical Bragg fibres, electro-mechanical impedance, etc.), are expensive [8,10] (optical Bragg fibres) or quite insensitive until a threshold value is reached [4] (dynamic modal data).

Ultrasonic Lamb waves, which were firstly described by Lord Horace Lamb [11] for homogeneous isotropic materials, have been studied over the last few decades [12–16] as a very attractive SHM method. Compared to other SHM approaches, those capitalizing on Lamb waves can offer a faster and more cost-effective evaluation of various types of damage. Lamb waves, i.e. elastic thickness waves, can reach relatively long distances (a few meters), even within materials with high attenuation ratios, allowing to cover wide inspection areas using few transducers. Being susceptible to both surface and embedded structural damage, they were widely used to develop damage identification approaches for delaminations, holes, cracks/notches, corrosion, degradation of lap joints; an exhaustive review can be found in [3,17,18]. However, because at least two fundamental modes are synchronously involved and overlap each other and because of their dispersive behaviour [3], a captured Lamb wave signal is often complex to be interpreted. Consequently, many efforts are available in the literature [3,19,20] to isolate "pure" single propagation modes: most of them rely on mutual interactions of an array of appropriately located piezoelectric transducers in order to enhance a specific wave mode while the others are minimized. This approach, as reported by Su et al. [3], is often termed "multi-sensor mode tuning technique". Another difficulty in the application of Lamb waves consists in the fact that, propagating at fast velocities, wave packets reflected by structural boundaries[21] and geometrical discontinuities[22] can easily mask weaker damage-scattered wave packets. Lastly, Lamb waves are highly susceptible to environmental conditions that can alter both signal amplitudes and spectral components. Contamination mainly arises from temperature fluctuation[23–25], inhomogeneity and anisotropy of materials[26], high-frequency ambient noise and low-frequency structural vibration[3].

NDT capability is typically expressed, according to Berens' model [27], by means of "Probability of Detection" (POD) curves, where the probability of detection is a monotonic function of the flaw size. As significant outputs, the lower confidence bound and the $a_{90/95}$ parameter (identifying the flaw size detectable with a probability of 90% and a confidence of 95%) define the system capability. Here, the typical variability sources, involved in the measured outcome, are human factors, flaw morphology, acousto-elastic properties of the medium and so on, as illustrated in Figure 1. Differently, SHM systems deal with a sensor network permanently installed on a host structure, their POD will be affected by material properties (piezo-elements, host structure), sensor location, crack growth initiation, length and orientation and their performance will be time-dependent due to ageing effects, environmental factors, etc. Moreover, the setup and installation of the sensors is, today, not a consistent (i.e. not standardized) procedure and thus subjected to other sources of variability. Thus, a complete POD curve, mainly based on experimental data, is an awesome task. More experimental trials cannot be a solution because each measurement reflects the uniqueness of the coupon in terms of i.e. sensor installation, damage pattern, etc. Taking advantage of reliable numerical models, Mueller and Aldrin [28,29] proposed the implementation of Model-Assisted POD (MAPOD) approaches able of simulating the variability involved in a SHM approach, although numerical efforts and computational times can be prohibitive [30], as well. Alternatively, given the aforementioned source of variability, Chang [31] suggested a SHM quantification approach based on one representative component with full environment conditions for a hotspot monitoring application.

Then, in parallel to practical challenges dealing with environmental conditions like temperature fluctuations and improvements by larger sensor spacing through Phased Array techniques, another fundamental task deals with statistical modelling of data for SHM reliability quantification. For instance, recently Schubert Kabban et al.[32] proposed a linear mixed-effects statistical model to deal with dependent data, based on the MIL-HDBK-1823A [33] POD procedure. However, as well as Berens' original formulation [27], the model is limited to a single explanatory variable (like flaw size) and a linear prediction between the possibly transformed signal response (damage index) and the flaw characteristic. Nevertheless, many applications can benefit from more than one explanatory variable and the description by nonlinear functions, where appropriate [34–36].Currently, Janapati et al. [37] performed an exhaustive experimental-numerical sensitivity study on flawed aluminium coupons concluding that the variation in sensor-actuator installation (adhesive thickness, transducer location) as well as damage propagation (damage size, crack growth orientation) are the main factors affecting SHM response variability. From this point of view, the present research investigates the feasibility of application of the very recent "Multi-Parameter" Probability of Detection approach[35], developed within the traditional NDT field, to guided waves based structural health-monitoring. As a first attempt, a relatively simple configuration is studied: a cost-effective PZT network is surface mounted on flat plates made of an isotropic EN AW 5754 aluminium alloy. Different key factors contributing to define the variability of the process are taken into account: the surface mounting process, piezo-electric constants, flaw morphology and defect orientation with respect to the PZT network. Instead, in-situ factors like temperature variation or ageing effects were not yet included. Hence, the intrinsic capability of the approach is here treated, before considering the effect of application parameters like environmental and ageing effects. In general, in SHM, the traditional Berens' approach for quantifying the capability of a NDT inspection cannot be applied any longer since it requires, firstly, the linearity of responses and, secondly, against one independent variable. Therefore, since a minimum statistical sample size has to be guaranteed, several plates/coupons have to be prepared for each combination of key factors to be investigated. Here, instead, the optimal way of combing data by means of a MP-POD approach is followed, where experimental as well as numerical data are combined to establish a "Measured â vs. Modelled a" data plot summarizing all the influencing and uncertain factors. Finally, a "Master" POD curve can be established by means of which the dependence on any single factor can be recognized. It is worth remarking the present aim is not to reproduce a "real" actuation-reception strategy of the PZT network, but testing the adequacy of a MP-POD formulation in an ultrasonic Lamb Waves based SHM approach.

Lamb Waves propagation and flaw interaction in aluminium plates

To the aim of evaluating the suitability of a MP-POD approach in describing different actuation strategies and different reception modes for Lamb waves in plate-like structures, the experimental flaw scattered response from artificial notches was firstly characterized according to the scheme of Figure 2, in a similar way as proposed by Lu et al. [38]. This particular configuration was chosen because it is a compact solution and it allows covering and monitoring, in an efficient way, the whole region of interest around a prospective flaw. Considering sensors mounting, the piezoelectric transducers dedicated to actuation and to reception of both flaw reflected (Pulse-Echo technique, “PE”) and flaw transmitted waves (Pitch-Catch technique, “PC”) are highlighted by the capital letters A, R and T, respectively.

Given the two here-considered actuation-reception strategies, actuation paths are highlighted by black arrows, PE responses by red ones and PC responses by blue ones. In detail, the first actuation-reception modality (Figure 2 (a)) operates on a diagonal path between the actuator piezoelectric transducer and a pair of PE-PC receivers so that the angle of incidence θ_i, reception θ_r and transmission θ_t are varying all together between each experimental measurement. The latter configuration (Figure 2 (b)) deals, instead, with a fixed actuation, perpendicular to the flaw, and a polar scattered echo reception, so to study the signal amplitude distribution of Lamb Waves around a crack-like artificial defect. Following the experimental campaign, Lamb Wave propagation and echo responses were modelled by means of finite element analyses to establish a linear relationship between empirical and numerical echo responses, allowing the investigation of the considered MP-POD approach.

Experiments

Two nominally identical aluminium plates, whose dimensions are 500x500 mm^2 with a thickness of 2 mm, were set-up with a network of circular 5 mm diameter and 1 mm thick PZT transducers (PIC-255 [39] with wrapped electrodes) according to the layout highlighted in Figure 3 (a). PZT installation, Figure 3 (b), followed a well-established chemical-mechanical procedure according to strain gauges practice: firstly, contaminants (foreign particles, oily substances, etc.) are removed from the surface by a solvent. Then, the surface is roughen by means of growing finer sandpapers (up to 600 grade) and residuals removed again by a solvent. Lastly, PZT are bonded using a single component, cold curing Z70 cyanoacrylate adhesive [40]. Particularly, the dimensions of the plates and the positions of the PZT network array were studied in order to avoid as much as possible unwanted reflections, from geometrical boundaries, able to mask valuable responses. Moreover, a modelling clay [21] was also applied at all the edges of the tested plates to damp as much as the same possible unwanted geometrical echoes.

An artificial slot was realized by a blade cut, Figure 3 (b), as representative of a crack-like defect and its length was gradually increased up to 100 mm, with steps of 1, 2 and 10 mm within the intervals [0;10), [10;40) and [40;100] mm, respectively. Considering the location of transducers, the outer ring of Figure 3 (a)-(b) dealt with piezo-actuators, whereas the rings nearby the flawed area gave out PE and PC responses according to the different strategies of actuation and reception. Then, the well-known mode tuning effects due to the coupling between the host structure and PZT elements, described elsewhere by Giurgiutiu et al. [19], matched with an out-of-phase and an in-phase way of actuation [3,20], are combined in order to selectively enhance a specific wave mode [41]. The best combination of central frequency of actuation were identified as 50 and 280 kHz for A_0 and S_0, respectively. These values also agree with an appropriate frequency regime, from Lamb Waves dispersion curves, in order to excite just the needed wave propagation modes. In Figure 4, the dispersion curves, obtained by a stable eigenvalue-eigenvector Semi Analytical Finite Element (SAFE) formulation [42], are reported, as phase velocity and group velocity, coherently with the specified experimental material properties given in Table 1. In detail, three quadratic 1-D finite elements allowed to describe the wave-guide cross-section and were judged to be sufficient to model the 2 mm thickness of the considered aluminium plates. This number of elements follows the convergence studies by Bartoli et al. [42] and the considerations that higher number of elements are needed for a better approximation of Lamb Waves mode shape at higher frequency-thickness ranges ($f \cdot d > 2\ MHz \cdot mm$) [43]. The effective elastic moduli of the considered aluminium alloy, i.e. Young Modulus E and Poisson's ratio υ, were experimentally characterized by suitable tensile tests according to ASTM E8/E8M [44]. Ultrasonic bulk velocities for both longitudinal (C_l) and shear (C_s) waves were obtained using a Gilardoni 4 MHz, 0° longitudinal and 60° shear wave contact probes arranged in a PE technique on a similar aluminium block. The anti-symmetrical modes are indicated by the continuous red lines, while symmetrical modes by the blue ones; for completeness, the results from the numerical solution of Rayleigh-Lamb equations [3], as well as group velocity from experiments [45], are superimposed respectively with green circles and red and blue dots. As can be seen, numerical results by both SAFE and Rayleigh-Lamb analytical formulation are in close agreement with experimental evidence, thus justifying the choice of three finite elements through the thickness.

The phase and group dispersion curves point out a "cut-off frequency", $f_{cut-off}$, around 800 kHz, i.e. the value of actuating frequency below which only the three fundamental Lamb wave propagation modes can exist: the symmetric one S_0, the anti-symmetric one A_0

and the shear horizontal one SH_0. Moreover, below this frequency value, the dispersive behaviour of such fundamental modes is restrained, i.e. the velocity is almost constant, apart for the A_0 mode close to the frequency origin. Thus, to avoid the simultaneous presence of more than three fundamental modes, an excitation frequency lower than 800 kHz (50 and 280 kHz for A_0 and S_0 mode selection, respectively, as described above) is applied throughout the research work.

A Hanning windowed 3.5 cycles tone burst, from an Agilent 33220A arbitrary waveform generator, is powered up to 100 $V_{peak-peak}$ by means of a WMA-300 High Voltage Amplifier; data were recorded at 20 MSa/s through an Agilent MSO-X 3014A oscilloscope. Since SHM relies on comparisons of different states, i.e. between a pristine and a damaged configuration, a baseline signal, immediately after the installation of the PZT network, was acquired as the reference condition for PE and PC responses as illustrated by the black solid lines shown in Figure 5 (a)-(d). All the recorded A-scans, i.e. baseline (black solid lines) and damaged conditions (red dashed lines), were suitably post-processed as follows:

1. raw data were firstly elaborated using the discrete wavelet transform (DWT) for de-noising the signal. In particular, Figure 5 (e), the Daubechies 4th level “db4” wavelet [46] proved to be particularly effective;

2. then, the signals were treated by the Hilbert transform, Figure 5 (e), so to draw them in the time domain and in terms of their energy content (envelope of the wave packet).

Finally, in order to quantify and compare PE and PC responses obtained from artificial notches, showed in Figure 5 (a)-(d), two very simple Damage Indexes (DI) were defined by means of a reflection coefficient R as:

$$R = \frac{max[A_{reflected}(t) - A_{baseline}(t)]}{\max[A_{baseline}(t)]} \tag{1}$$

and a reflection coefficient T as:

$$T = \frac{max[A_{transmitted}(t)]}{max\ \ [A_{baseline}(t)]} \tag{2}$$

where $A_{reflected}(t)$, $A_{transmitted}(t)$ and $A_{baseline}(t)$ stand for the envelope amplitude of the first captured damage-reflected, -transmitted and baseline wave components, respectively. Defining reflection and transmission coefficients with respect to the input incident signal (baseline), which was the same for all measurements, a normalization (scaling) of the data was performed without losing useful information about the amplitude ratios between all of the acquired responses. In particular, the captured signal falls within a specified range like (-1; +1) effectively avoiding data distortion and making different signals more easily managed and compared[3]; moreover, variations in material parameters, like sensor, structural and adhesive properties are cancelled out from DI responses [37].

The defined post-processing procedure was applied to all the data recorded by both the "diagonal actuation-reception" strategy and the "normal incidence polar reception" way around. PE and PC results from the two different actuation-reception strategies, and dealing with the fundamental A_0 and S_0 modes, are summarized in Figure 6 and Figure 7. A detailed discussion on the obtained results is provided in a dedicated Section later on, but it is here worth noting the influence of experimental uncertainties on responses. In particular, both figures show, for each test configuration and with the same colours, the results obtained by the two nominally identical tested plates: as can be seen, the trends are qualitatively in close agreement, but the quantitative response values are generally different. This seems to suggest the importance of a statistical analysis of SHM results in order to define the capability of the approach. Therefore, for a hotspot monitoring application (where the approximate damage location and orientation are known), testing of multiple coupons may not be necessary in order to apply a traditional POD-based analysis, at least under the assumption of accurate sensor installation, appropriate compensation of the environmental and boundary conditions effects and compensation of aging effects. Numerical simulations, through calibrated numerical models, can help to minimize the number of components required for estimating POD for SHM systems.

Finite Element Modelling

3D finite element analyses were carried out using the explicit dynamic formulation of Abaqus CAE 6.13.1 [47], a computationally efficient way for solving large 3D dynamic problems, like ultrasonic wave propagation [18]. On the other hand, piezoelectric elements are not supported by Abaqus' explicit solver and, consequently, the multi-physics behaviour due to electro-mechanical coupling effects of PZT and host structure had to be neglected. Hence, actuation is here modelled, similarly to Mustapha and Ye[48], applying in-plane radial displacements on the peripheral nodes corresponding to the PZT diameter, as described in Figure 8 (a), even if this approach is somehow an approximation with respect to multi-physics. Moreover, in-plane displacements directly prescribed on the nodes of the PZT elements, instead of shear/concentrated forces[38,49], reduce computational time.

The employed structured mesh in Figure 8 (b) uses eight nodes linear elements with reduced integration (C3D8R), with a plane dimension of 2 mm and an aspect ratio of two, allowing two elements along the thickness. In this way, regarding the here investigated frequency ranges equal to $50\ kHz$ for A_0 and $280\ kHz$ for S_0, 10 elements per wavelength λ are roughly employed, thus satisfying the usual [18] minimum requirement of eight elements per wavelength, when using linear elements. In addition, two linear elements per thickness was sufficiently accurate to describe Lamb Wave mode shapes within this frequency range [18]; more elements along the thickness should be used at higher frequency due to higher complex patterns [43].

Lastly, since the explicit scheme is conditionally stable, a rough stability upper limit [47] was determined as:

$$\Delta t < \frac{\Delta x}{C_l} \tag{3}$$

where Δt is the integration time step, Δx the smallest element size and C_l the dilatational wave speed, equal to 6300 m/s for an aluminum alloy. A compromise [50] between accuracy and computational times was found using 20 points per cycle of the highest frequency component. A stable time integration step was, then, here set to 5e-8 s, corresponding to a sampling rate of 20 MSa/s. The linear and quadratic bulk viscosity coefficients [47], introduced by default by Abaqus' explicit solver to control high frequency oscillations ("ringing") and to prevent collapsing of elements due to high velocity gradients from shock wave propagations, respectively, were set to zero.

An artificial crack-like flaw was introduced (Fig. 8 (c)) removing the finite elements associated to the width of the blade cut. Thus, with an overall of 127142 brick elements and 576885 degree of freedoms, each explicit dynamic simulation took 156 s on a 16GB RAM, Intel Core i5-4670 CPU personal computer.

An example of FEM output is reported in Figure 9, where the scattered response from a 20 mm long artificial defect, interacting with orthogonal and 45°incident A_0 and S_0 modes, is highlighted by means of magnitude displacement contour plots. For the previously stated reason, a direct comparison of the data (mV from experiments and displacement amplitudes from FEM) was impossible. Hence, from similar frames and different notch sizes, the nodal out-of-plane displacement U_3 for A_0 mode and the magnitude of in-plane components U_1, U_2 for S_0 mode were adopted as the A-scan flaw scattering response. As well as done for experimental data, also numerical results were scaled with respect to their incident incoming wave and the previously described signal post-processing procedure was applied.

Discussion on experimental and numerical results

Pulse Echo Response

Experimental flaw scattering responses from 1 mm to 100 mm long notches under varying incidence θ_i-reception θ_r paths are illustrated in Figure 10 for A_0 $(50kHz)$ and

S_0 $(280kHz)$ interrogation modes. Starting from the reflected components, three peculiarities can be highlighted. Firstly, it is worth noting that, contrarily to what generally expected and apart from saturation effects, in the case of normal incidence and reception path, the wave scattered amplitude is differently increasing, with flaw size, with respect to a simple linear monotonic trend. In particular, the response showed a linear trend up to approximately 60 mm notch length, in agreement with a high frequency approximation, and then it started to oscillate. This peculiar behaviour, observed by Lu et al.[51] under oblique–incident Lamb waves interaction, it is attributed in the literature[52] to the superposition of directly scattered and crack tip diffracted waves. A similar oscillating behaviour was also observed in a study carried out by Peng et al.[53] dealing with delamination on a carbon fibre composite laminate. Secondly, a reasonable and stable echo response is recorded only above 10 mm notch length, a length that corresponds to half the wavelength of both the 50 kHz A_0 mode and the 280 kHz S_0 one. This is in agreement with the general rule of thumb [54] for which a discontinuity must be larger than one-half the wavelength to stand a reasonable chance of being detected. Thirdly, the reflection coefficient decreases significantly with increasing the angle of incidence-reception. This is directly related to the here-chosen experimental set-up and will be explained in detail in a following Section.

Regarding experimental wave scattered components under a normal incidence actuation, data in terms of reflection coefficient are summarized in Figure 11, as a function of flaw size, for both A_0 and S_0 modes. Comments similar to those just reported for the previous case can be done, but it is generally evident that significantly higher reflected echo amplitudes are recorded with respect to those collected under variable incidence-reception angles, where sensors were exactly aligned along the propagation path of incident waves. Comparing numerical and experimental PE results, from a qualitative point of view, the trends are in good agreement: the same continuous non-monotonic functions against the flaw size are highlighted. Particularly, numerical values match perfectly to experimental ones regarding the S_0 mode, while a rather good agreement is found for A_0 mode. Given the fact that nodal displacements and output voltage of a PZT are proportional to each other, the observed differences can be attributed to the discrepancies between the FE model and the real host structure, i.e. to damping, electro-mechanical coupling, residual mode excited by dual actuators in experiment, crack shapes (Figure 8 (c)), etc. Anyway, considering the final aim of establishing a MP-POD formulation, a linear correlation between measured and modelled amplitudes must be found in order to apply Berens' statistical framework and, consequently, to establish a "Master" POD curve. Only if huge deviations from a linear behaviour are observed, the model is not taking into account the physics of the problem and, thus, has to be re-formulated. On the other hand, if a linear trend is found and modelled data are only rigidly translated either lower or higher than the expected behaviour, it means a constant calibration factor is missing.

Pitch Catch Response

Regarding experimental PC responses, the transmitted components according to transmission coefficients are recapped in Figures 12 and 13. Starting from diagonal actuation-reception paths, an increase of the transmission coefficient with respect to θ_i is pointed out, together with a decrease with the flaw size, as it could be expected to the presence of a shadow zone[51]. A peculiarity, instead, is highlighted at 90° for the A_0 $(50\ kHz)$ mode, where the transmission coefficient initially starts from a value of 1.0 to end up with an increase of transmitted amplitude with flaw size. As stated by Y. Lu et al. [51], this behaviour is mostly attributable to the destructive or constructive interference resulting from the superposition of incident and diffracted Lamb waves from crack tips [52], leading to an enhancement or weakening of the collected response far away from the crack. In the present case, diffraction effects enhanced the recorded response allowing the transmission coefficient to exceed unity.

Differently, flaw scattered responses collected under normal incidence are characterized by strong fluctuations both for low and high reception angles (Fig. 13) as a superposition of directly scattered and crack tip diffracted waves.

As well as in the PE reception mode, also in this case numerical flaw scattered responses are in good agreement with experimental evidence: the general behaviour as well as fluctuations in transmitted echo amplitudes are well captured by the proposed FE analysis. In particular, the agreement is somewhat better, especially for some reception angles, with respect to PE. This can be explained by the fact that defining a transmission coefficient, and thus identifying its corresponding wave component, it is easier than dealing with reflected wave components where at least two fundamental modes plus the shear horizontal one SH_0 can coexist. Even though the mode tuning effect coupled with an out-of-phase/in-phase actuation of a pair of PZT was applied, unwanted wave modes can be only minimized and not completely cancelled out as in FE simulations.

Prospective effectiveness of “diagonal” and “normal incidence” techniques

A final comment deals with what would happen to the R and T coefficients if crack size went on growing. Generally speaking, a saturated response is expected when crack grows to a dimension larger than the region monitored by the experimental set-up.

Figure 10 seems to suggest the diagonal actuation-reception technique would tend to saturate at R=1 for angles up to 30°, while for higher angles it would remain rather low and close to R=0. At the same time, Figure 12 shows the T coefficient always tends to T=0 with crack growth. These conclusions are also supported by the intuition a big (saturated) reflector reflects the entire sound energy so that no transmission takes place and the reflected direction is, according to Snell's Law[51], symmetrical to the incident one with respect to the line perpendicular to the notch. In these terms, an effective reception would be achieved positioning PE sensors mirrored with respect to the configuration chosen for the present research.

Considering the normal incidence with polar reception technique, Figure 11 suggests a saturation at R=1 for angles up to about 90°, while at exactly 90° it would remain rather low and close to R=0. At the same time, Figure 13 shows the T coefficient always tends to T=0 with crack growth for angles up to about 90°, while at 90° it would remain very high at T=1. The rationale behind this behaviour is the same about big reflectors and Snell's Law already described for the diagonal actuation-reflection technique.

All these observations suggest the arrangement of the PZT network is definitely critical for defect detection. For the here-considered set-ups, the best performance is obtained by the normal incidence with polar reception technique, which, on the other hand, is more expensive than the diagonal actuation-reception because requires a higher number of sensors. Nevertheless, it must be remembered that the position, size and orientation of flaws could be rarely known in advance in real applications and so the best experimental set-up is an unknown of the problem. From this point of view, a capability study of the SHM network would effectively benefit from a MP-POD approach, expressing its capability against the influencing factors.

Multi-Parameter POD assessment

A Multi-Parameter POD approach allows for the description of the probability of detection of a system against different relevant factors like flaw size (typical POD linear characteristic in Berens' model), orientation, position, etc. The mathematical procedure relies on applying Berens' algorithm to the measured amplitude, $\hat{a}$, as a function of a modelled one, a, providing an optimal combination of all intrinsic influencing parameters. Then, a "Master" POD curve is obtained as a function of modelled data. Since the model itself gives the relationship between the signal response and the influencing parameters, it is then possible to calculate a POD curve as a function of the single involved parameters. In particular, the following uniqueness are addressed. Firstly, differently to the traditional model, in which the linearity between the signal and the influencing parameter is assumed just by observing the measured data set or from suitable transformation of the data ($log - log, d^2, \ldots$), the relationship in the multi-parameter model comes from the simulation representing our understanding of the underlying physics of the process. Thus, a first assessment of the goodness of the model can be defined. Then, as a natural consequence, non-linear responses, as those considered here, can be linearized through the “Measured â vs. Modelled a” diagram, and thus it is possible to get back to the conventional Berens’ statistical framework. On the subject, a parametric physics based model has always to be preferred and is usually more efficient requiring the minimum number of parameters to describe the response. Furthermore, as stated by C. Annis et al. [55], it: “*produces a more believable description of the underlying reality and does not tempt the unwary into trying to explain group differences that are only illusory”.* The here considered deterministic factors are flaw size, a, orientation with respect to the PZT network, $\theta_i - \theta_r$ and the Lamb mode, $A_0 - S_0$, whereas the surface installation, piezo-electric properties, cabling, etc. are included within random factors. The former factors give the slope and intercept of the regression between experimental and numerical amplitudes, while the latter give the overall variability (dispersion) around the mean value. The MP-POD formulation is reported in Figure 14 for the PE flaw scattered responses: Figure 14 (a)-(b) deal with the “Measured â vs Modelled a” diagrams and Figure 14 (c)-(d) with the related Master POD curves for A_0

and S_0 modes, respectively. With black and red dots, the response from diagonal actuation-reception paths and normal incidence-polar reception paths is characterized.

In an ideal case, where all the influencing parameters are included in the model, “Measured â vs. Modelled a” data should lie on a 45° line. This behaviour is clear for the fundamental S_0 mode, where the magnitude of in-plane displacements were used as the numerical flaw scattered response. On the contrary, the anti-symmetrical A_0 mode is characterized by an excellent agreement between experimental and numerical responses for all the here investigated actuation-reception strategies, the latter aspect pointed out by the clear linear trend, even though the numerical flaw scattered response, based on the out-of-plane displacement, is somewhat underestimated. Bearing in mind that for the MP-POD formulation, more than following the ideal 45° line, the linear behaviour is a necessary and sufficient condition to establish a Master POD curve, amplitudes differ of a model factor, roughly 12.5%, to calibrate the modelled data to the experimental ones. Then, the estimate of the linear regression parameters is established by the well-known Maximum Likelihood Estimation (MLE) able of taking into account for censored data. The latter are the data either below the level of noise or above the saturation level of the chain-measurement setup; in our case, the mean level of noise was expressed in terms of a reflection factor, coherently to the defined DI, and established as 5% of the screen amplitude. Due to the linearity of response, the homoscedasticity and the normality of residuals, it is possible to formulate a “Master” POD curve, as showed in Figure 14, as a function of the numerical reflection coefficient. The latter, taking into account different combinations of parameters, allows splitting the “Master” POD curve into the individual factors, as showed in the following subsections. The decision threshold for the definition of the POD curve was here simply set equal to three times the maximum noise amplitude; discussion about threshold level definition for an effective decision-making procedure can be found in [56]. It’s worth noting that the same concepts and formulation can be extended, but here neglected for the sake of brevity, to transmitted amplitudes, as long as a linearity between experimental and a physics based numerical response is highlighted.

MP-POD curves for diagonal actuation-reception paths

Dealing with the diagonal actuation-reception configuration of Figure 2 (a), where the angle of incidence and reception is ranging from 0° to 90°, from the Master POD curves for A_0 and S_0 modes reported in Figure 14 (c)-(d), it is possible to derive POD curves as a function of the flaw size and actuation-reception angles as showed in Figure 15.

As observed in the experimental scattered response, when incident Lamb waves are tilted with respect to the crack surface normal vector, the amplitude of the reflected waves received by the sensor is considerably lower. The effect of an off-axis orientation, with respect to flaw position, is well reflected by the POD of Figure 15 (a)-(b) where it states a detectable $a_{90/95}$ flaw size equal to 13.8 mm, for A_0 and 17 mm, for S_0; hence, the fundamental A_0 mode is somewhat 20% more performant than S_0 one. These values are achievable and can be defined only for a normal incidence reception path: incidence-reception paths also slightly away from the normal condition will lead to severely right hand shifted POD, where a $a_{90/95}$ parameter cannot be defined any longer. This is a valuable information that cannot be pointed out by a simple observation of the experimental data, as in Figure 10 through Figure 13. It is worth noting that, except from actuation and reception angle of 0°, POD curves significantly differ from a traditional monotonic trend, but minima and maxima can be highlighted leading to regions of better or worse detectability.

MP-POD curves for normal incidence with polar reception paths

The same previously discussed mathematical framework is now applied for the second considered configuration of normal incidence and polar reception paths as shown in Figure 2 (b). So, experimental data were firstly represented in $\hat{a}\ vs.a$ plot against modelled ones, as shown in Figure 14. Subsequently, once verified the implicit statistical assumptions in regression analysis, a “Master” POD curve can be built and, finally, a POD against flaw size and different reception paths (i.e. orientation angle of PZT with respect to the normal defining crack position) expressed as in Figure 16 (a)-(b). Once again, POD curves are defined with respect to a decision threshold equal to three times the noise level. Regarding the A_0 mode, the classical monotonic S-Shape function is outlined for reception angle of 0°, whereas for off-axis angle POD curves they are affected by strong oscillations, and is some cases, $\theta_r = 60°, \theta_r = 90°$, they will never converge to one, in agreement with the physical behaviour underlined by FEM and experiments. Particularly, dealing with $\theta_r = 30°$ and starting from 10 mm notch length, POD grows up to 1 and then immediately drops down in a negative trend to 0.6; only above 40 mm notch length, the classical trend is re-established. The aforementioned trends are less evident working with the S_0 mode, even if it's worth pointing out that as well as the general behaviour states POD generally lower, for all reception angles and small crack sizes, as increasing the crack length the POD will reach the same performance of the A_0 mode. Hence, concerning the $a_{90/95}$ parameter, substantially there is no significant difference choosing a particular fundamental mode regarding a through passing crack as long as the incidence and reception paths are normal to the crack surface. For higher off-axis reception angles, the A_0 mode seems to be more sensitive, especially at smaller crack sizes as showed in Figure 17. Finally, it is interesting to point out that a POD value greater than 0 can be found for defect sizes starting from 10 mm. Again, this is an overall tendency related to well-known rule of thumb that the wavelength, roughly equal to 10 mm both for A_0 at 50 kHz and S_0 at 280 kHz, has to be less than two times the crack size.

Concluding remarks

The authors investigated the feasibility of a Multi-Parameter POD approach, developed within the NDT field, combining experimental and numerical results for a SHM Lamb Waves based approach. Although as a preliminary study and not concerning all sources of variability, the approach and results seem encouraging. Particularly, its formulation allows the application of the conventional statistical framework used in the field of NDT capability, taking advantage of describing the influence of various factors by only one explanatory variable. Consequently, useful characteristic can be extracted especially when a refinement of Lamb Waves sensitivity is needed. It is advantageous when highly nonlinear response concurs defining the overall response, as well, and every time a parametric model can be of difficult application and/or without any physical meaning.

Once established the “Master” POD curve of the system, it can be split into the single influencing factors like crack size, orientation, etc. Concerning the experimental setup, it is underlined that the POD curve can be a non-monotonic function of crack size, but oscillations are present compatibly to the physical behaviour highlighted by both numerical simulations and experimental data. Then, it is pointed out that a low frequency diagnostic wave, mainly concentrated in the A_0 mode, can carry the same amount of sensitivity of a passing through crack, with respect to higher ones using S_0 mode. Such a conclusion is consistent with the fact that the wavelength of the two fundamental modes is approximately the same. Lastly, it is worth noting that, under strict assumptions, multiple coupons may not be necessary for hotspot monitoring applications and calibrated numerical models could be used for estimating the POD. In this light, calibration and adequacy of numerical models can be decided by a linear relationship within MP-POD "Measured â vs. Modelled a" data plot, while the intrinsic variability is defined by experimental data and not fictitiously by simulations.

Acknowledgments

The authors would like to thank Mr. F. Ramponi for the fundamental help on experimental tests. The present research has been carried out in the frame of the "PoliNDT" interdisciplinary lab set at Politecnico di Milano. Lastly, the present paper is a development of a preliminary version selected from the 16th AIPnD Conference (Milan, Italy, 2015).

Declaration of Conflicting Interests

The Authors declare that there is no conflict of interest.

References

1. Boller C. Ways and options for aircraft structural health management. *Smart Mater Struct* 2001; 10: 432–440.
2. Staszewski W, Boller C, Tomlinson GR. *Health Monitoring of Aerospace Structures: Smart Sensor Technologies and Signal Processing*https://books.google.it/books/about/Health_Monitoring_of_Aerospace_Structure.html?id=WHjoo6VdBHMC&pgis=1 (2004, accessed 9 January 2016).
3. Su Z, Ye L. *Identification of Damage Using Lamb Waves: From Fundamentals to Applications*. Springer Science & Business Mediahttps://books.google.com/books?id=jvzkoGBwBl0C&pgis=1 (2009, accessed 9 January 2016).
4. Rolek P, Bruni S, Carboni M. Condition monitoring of railway axles based on low frequency vibrations. *Int J Fatigue* 2016; 86: 88–97.
5. Roth W, Giurgiutiu V. Adhesive disbond detection using piezoelectric wafer active sensors. In: Shull PJ (ed). International Society for Optics and Photonics, p. 94370S.
6. Cawley P. The sensitivity of the mechanical impedance method of nondestructive testing. *NDT Int* 1987; 20: 209–215.
7. Gutkin R, Green CJ, Vangrattanachai S, et al. On acoustic emission for failure investigation in CFRP: Pattern recognition and peak frequency analyses. *Mech Syst Signal Process* 2011; 25: 1393–1407.
8. Bernasconi A, Carboni M, Comolli L, et al. FATIGUE CRACK GROWTH MONITORING IN COMPOSITE BONDED LAP JOINTS BY A DISTRIBUTED FIBER OPTIC SENSING SYSTEM AND COMPARISON WITH ULTRASONIC TESTING. *J Adhes* 2015; 00218464.2015.1123153.
9. Sbarufatti C, Manes A, Giglio M. Application of sensor technologies for local and distributed structural health monitoring. *Struct Control Heal Monit* 2014; 21: 1057–1083.
10. Bernasconi A, Comolli L. An investigation of the crack propagation in a carbon fiber bonded joint using backface strain measurements with FBG sensors. In: Liao Y, Jin W, Sampson DD, et al. (eds) *OFS2012 22nd International Conference on Optical Fiber Sensor*. International Society for Optics and Photonics, p. 84214Y–84214Y–4.
11. Lamb H. On Waves in an Elastic Plate. *Proc R Soc A Math Phys Eng Sci* 1917; 93: 114–128.
12. Su Z, Ye L. Lamb wave-based quantitative identification of delamination in CF/EP composite structures using artificial neural algorithm. *Compos Struct* 2004; 66: 627–637.
13. Seth S. Kessler SMSCS. Damage Detection in Composite Materials using Lamb Wave Methodshttp://citeseerx.ist.psu.edu/viewdoc/summary?doi=10.1.1.493.708 (accessed 9 January 2016).
14. Biemans C, Staszewski WJ, Boller C, et al. Crack Detection in Metallic Structures Using Piezoceramic Sensors. *Key Eng Mater* 1999; 167-168: 112–121.
15. Valle C, Littles JW. Flaw localization using the reassigned spectrogram on laser-generated and detected Lamb modes. *Ultrasonics* 2002; 39: 535–542.
16. Silva MZ, Gouyon R, Lepoutre F. Hidden corrosion detection in aircraft aluminum structures using

laser ultrasonics and wavelet transform signal analysis. *Ultrasonics* 2003; 41: 301–305.

17. Su Z, Ye L, Lu Y. Guided Lamb waves for identification of damage in composite structures: A review. *J Sound Vib* 2006; 295: 753–780.
18. Rose JL. *Ultrasonic Guided Waves in Solid Media*. Cambridge University Presshttps://books.google.com/books?id=UWfwAwAAQBAJ&pgis=1 (2014, accessed 9 January 2016).
19. Giurgiutiu V. Tuned Lamb Wave Excitation and Detection with Piezoelectric Wafer Active Sensors for Structural Health Monitoring. *J Intell Mater Syst Struct* 2005; 16: 291–305.
20. Kim SB, Sohn H. Instantaneous reference-free crack detection based on polarization characteristics of piezoelectric materials. *Smart Mater Struct* 2007; 16: 2375–2387.
21. Calomfirescu M. *Lamb Waves for Structural Health Monitoring in Viscoelastic Composite Materials*. Logos-Verlaghttps://books.google.it/books?id=_p6muhkbVB0C (2008).
22. Lanza di Scalea F, Rizzo P, Marzani A. Propagation of ultrasonic guided waves in lap-shear adhesive joints: Case of incident a[sub 0] Lamb wave. *J Acoust Soc Am* 2004; 115: 146.
23. Clarke T, Simonetti F, Cawley P. Guided wave health monitoring of complex structures by sparse array systems: Influence of temperature changes on performance. *J Sound Vib* 2010; 329: 2306–2322.
24. Croxford AJ, Moll J, Wilcox PD, et al. Efficient temperature compensation strategies for guided wave structural health monitoring. *Ultrasonics* 2010; 50: 517–528.
25. Roy S, Lonkar K, Janapati V, et al. A novel physics-based temperature compensation model for structural health monitoring using ultrasonic guided waves. *Struct Heal Monit* 2014; 13: 321–342.
26. Willberg C, Koch S, Mook G, et al. Continuous mode conversion of Lamb waves in CFRP plates. *Smart Mater Struct* 2012; 21: 075022.
27. Berens AP. NDE Reliability Data Analysis. In: *ASM Handbook Volume 17, Nondestructive Evaluation and Quality Control (ASM International)*. 1989, pp. 689–701.
28. I. M, Janapati S, Banerjee S, et al. On the performance quantification of active sensing SHM systems using model assisted POD methods. In: DEStech Publications, Lancaster P 17602 U (ed) *Proceedings of the Eighth International Workshop on Structural Health Monitoring*. Stanford, CA, 2011, pp. 2417–2428.
29. Aldrin JC, Medina EA, Lindgren EA, et al. CASE STUDIES FOR MODEL-ASSISTED PROBABILISTIC RELIABILITY ASSESSMENT FOR STRUCTURAL HEALTH MONITORING SYSTEMS. In: *REVIEW OF PROGRESS IN QUANTITATIVE NONDESTRUCTIVE EVALUATION: Volume 30A; Volume 30B*. AIP Publishing, pp. 1589–1596.
30. Stepinski T, Uhl T, Staszewski W. *Advanced Structural Damage Detection*. Chichester, UK: John Wiley & Sons, Ltd. Epub ahead of print 17 June 2013. DOI: 10.1002/9781118536148.
31. Chang FK. The need of SHM Quantification for Implementation. *EWSHM - 7th European Workshop on Structural Health Monitoring*http://memsic.ccsd.cnrs.fr/EWSHM2014/hal-01010064 (2014, accessed 20 May 2016).
32. Schubert Kabban CM, Greenwell BM, DeSimio MP, et al. The probability of detection for structural health monitoring systems: Repeated measures data. *Struct Heal Monit* 2015; 14: 252–264.
33. MIL-HDBK-1823A:2009. Nondestructive Evaluation System Reliability Assessment Department of Defense Handbook: nondestructive Evaluation System Reliability Assessment.
34. Carboni M, Cantini S. a New Approach for the Definition of ‘Probability of Detection’ Curves. *Ecndt*http://www.ndt.net/search/docs.php3?DocGroup=-1&date (2010).
35. Pavlovic M, Takahashi K, Müller C. Probability of detection as a function of multiple influencing

parameters. *Insight - Non-Destructive Test Cond Monit* 2012; 54: 606–611.

36. Yusa N, Chen W, Hashizume H. Demonstration of probability of detection taking consideration of both the length and the depth of a flaw explicitly. *NDT E Int* 2016; 81: 1–8.
37. Janapati V, Kopsaftopoulos F, Li F, et al. Damage detection sensitivity characterization of acousto-ultrasound-based structural health monitoring techniques. *Struct Heal Monit* 2016; 15: 143–161.
38. Lu Y, Ye L, Su Z, et al. Quantitative evaluation of crack orientation in aluminium plates based on Lamb waves. *Smart Mater Struct* 2007; 16: 1907–1914.
39. Technology P. Piezoelectric Ceramic Products. 2014, p. 44.
40. GmbH HBM. Scheda di dati di sicurezza. 2013; 1–10.
41. Carboni M, Gianneo A, Giglio M. A Lamb waves based statistical approach to structural health monitoring of carbon fibre reinforced polymer composites. *Ultrasonics* 2015; 60: 51–64.
42. Bartoli I, Marzani A, Lanza di Scalea F, et al. Modeling wave propagation in damped waveguides of arbitrary cross-section. *J Sound Vib* 2006; 295: 685–707.
43. Ahmad Z a. B, Vivar-Perez JM, Gabbert U. Semi-analytical finite element method for modeling of lamb wave propagation. *CEAS Aeronaut J* 2013; 4: 21–33.
44. ASTM E8. ASTM E8/E8M standard test methods for tension testing of metallic materials 1. *Annu B ASTM Stand 4* 2010; 1–27.
45. Gianneo A. *Advanced Reliability Aspects of Non Destructive Testing (NDT) and Structural Health Monitoring (SHM): Probability of Detection, Multi-Parameter-POD and Model-Assisted POD Formulation*. Politecnico di Milano, 2016.
46. Debnath L. *Wavelets and Signal Processing*. Springer Science & Business Mediahttps://books.google.com/books?id=oPf2BwAAQBAJ&pgis=1 (2012, accessed 9 January 2016).
47. ABAQUS Inc. Abaqus 6.13.1, User's Manual.
48. Mustapha S, Ye L. Leaky and non-leaky behaviours of guided waves in CF/EP sandwich structures. *Wave Motion* 2014; 51: 905–918.
49. Mustapha S, Ye L, Dong X, et al. Evaluation of barely visible indentation damage (BVID) in CF/EP sandwich composites using guided wave signals. *Mech Syst Signal Process* 2016; 76: 497–517.
50. Moser F, Jacobs LJ, Qu J. Modeling elastic wave propagation in waveguides with the finite element method. *NDT E Int* 1999; 32: 225–234.
51. Lu Y, Ye L, Su Z, et al. Quantitative assessment of through-thickness crack size based on Lamb wave scattering in aluminium plates. *NDT E Int* 2008; 41: 59–68.
52. Rajagopal P. Interaction of the Fundamental Shear Horizontal Mode with a Through Thickness Crack in an Isotropic Plate. In: *AIP Conference Proceedings*. AIP, pp. 157–164.
53. Peng H, Ye L, Meng G, et al. Concise analysis of wave propagation using the spectral element method and identification of delamination in CF/EP composite beams. *Smart Mater Struct* 2010; 19: 11.
54. Krautkrämer J, Krautkrämer H. *Ultrasonic Testing of Materials*. Springer-Verlag Berlin Heidelberg. Epub ahead of print 1990. DOI: 10.1007/978-3-662-10680-8.
55. Annis C, Aldrin JC, Sabbagh HA. NDT Capability. *Mater Eval* 2015; 73: 44–54.
56. Memmolo V, Maio L, Boffa ND, et al. Damage detection tomography based on guided waves in composite structures using a distributed sensor network. *Opt Eng* 2015; 55: 011007.

List of Tables

Table 1

$\boldsymbol{E}\ [\boldsymbol{GPa}]$	$\boldsymbol{\nu}$	$\boldsymbol{\rho}\ [\frac{\boldsymbol{kg}}{\boldsymbol{m}^3}]$	$\boldsymbol{C_l}\ [\frac{\boldsymbol{m}}{\boldsymbol{s}}]$	$\boldsymbol{C_t}\ [\frac{\boldsymbol{m}}{\boldsymbol{s}}]$
71.5	0.33	2670	6370	3160

List of Figures

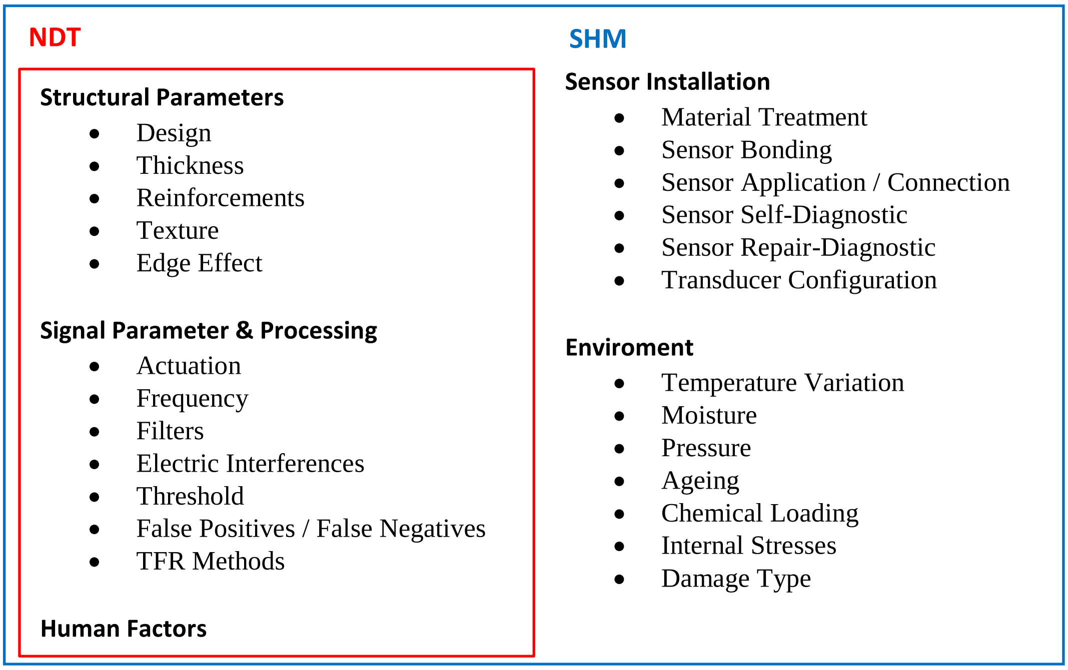
NDT
Structural Parameters
Design
Thickness
Reinforcements
Texture
Edge Effect
Signal Parameter & Processing
Actuation
Frequency
Filters
Electric Interferences
Threshold
False Positives / False Negatives
TFR Methods
Human Factors
SHM
Sensor Installation
Material Treatment
Sensor Bonding
Sensor Application / Connection
Sensor Self-Diagnostic
Sensor Repair-Diagnostic
Transducer Configuration
Enviroment
Temperature Variation
Moisture
Pressure
Ageing
Chemical Loading
Internal Stresses
Damage Type

Figure 1

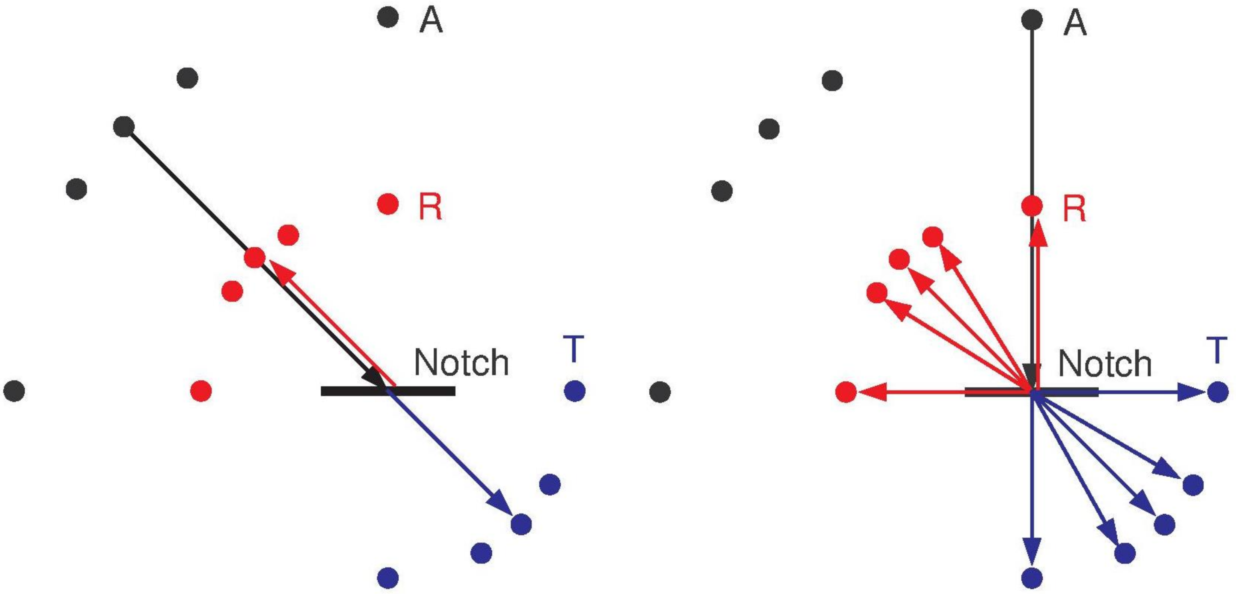

(a) (b)

Figure 2

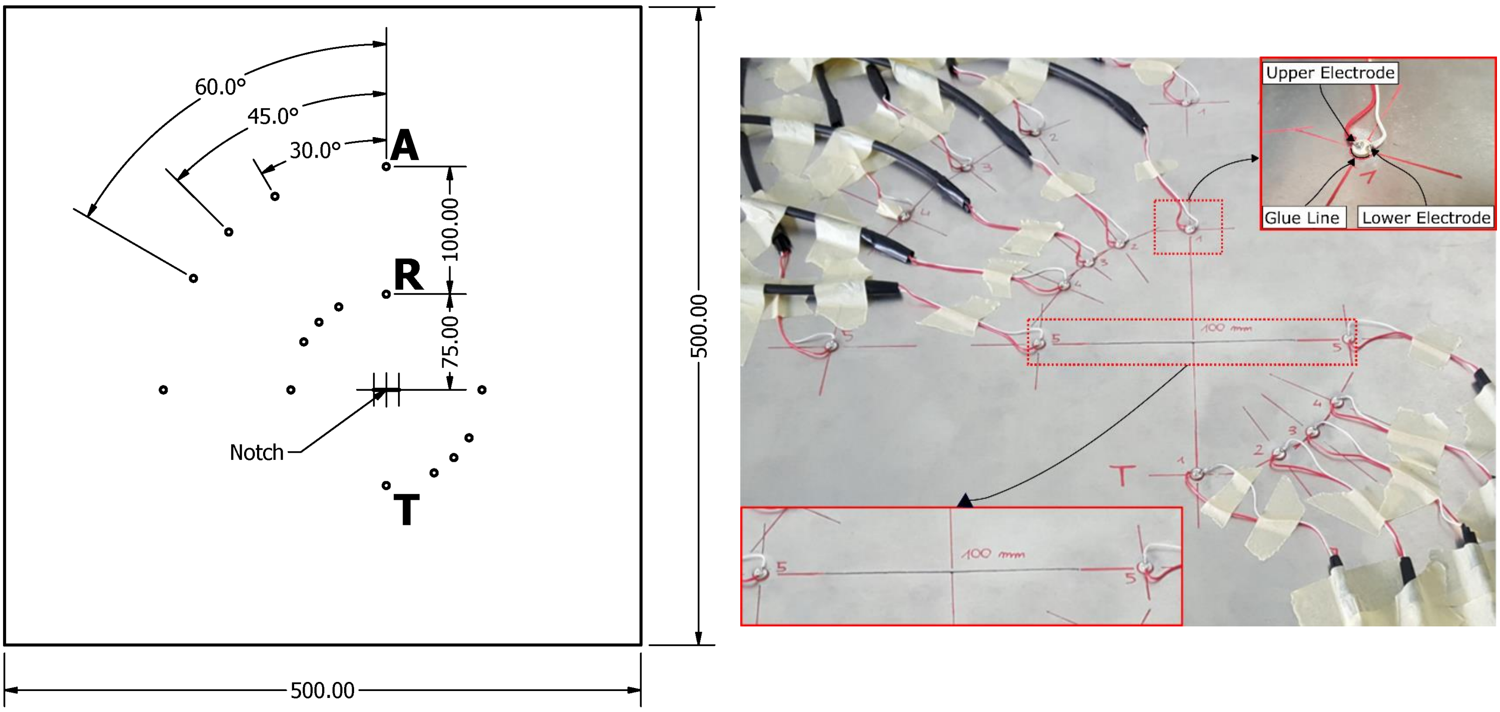
60.0°
45.0°
30.0°
A
R
T
100.00
75.00
500.00
500.00
Notch
Upper Electrode
Glue Line
Lower Electrode
100 mm
1
2
3
4
5

(a) (b)

Figure 3

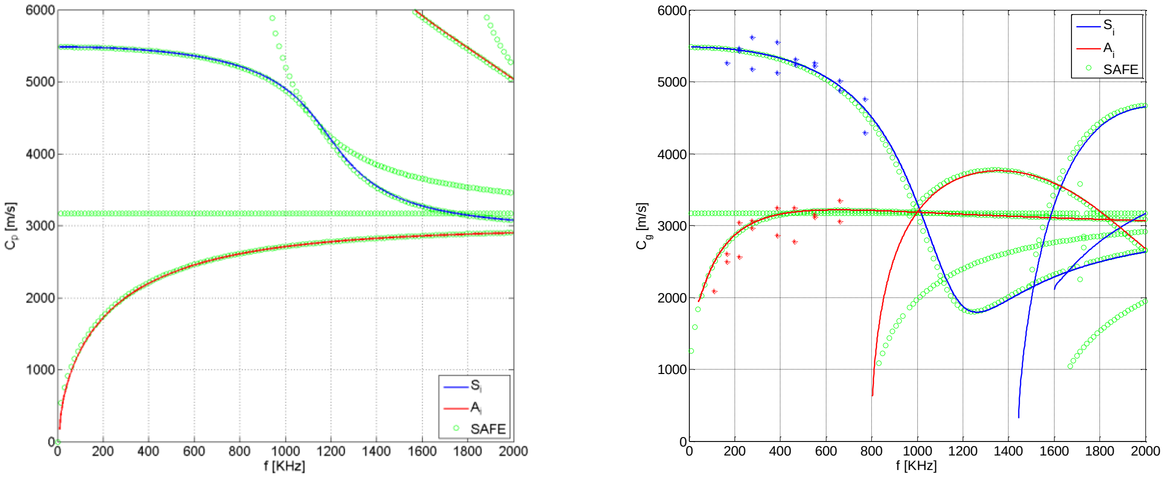
6000
5000
4000
3000
2000
1000
0
0
200
400
600
800
1000
1200
1400
1600
1800
2000
f [KHz]
C_p [m/s]
S_i
A_i
SAFE
6000
5000
4000
3000
2000
1000
0
0
200
400
600
800
1000
1200
1400
1600
1800
2000
f [KHz]
C_g [m/s]
S_i
A_i
SAFE

(a)

(b)

Figure 4

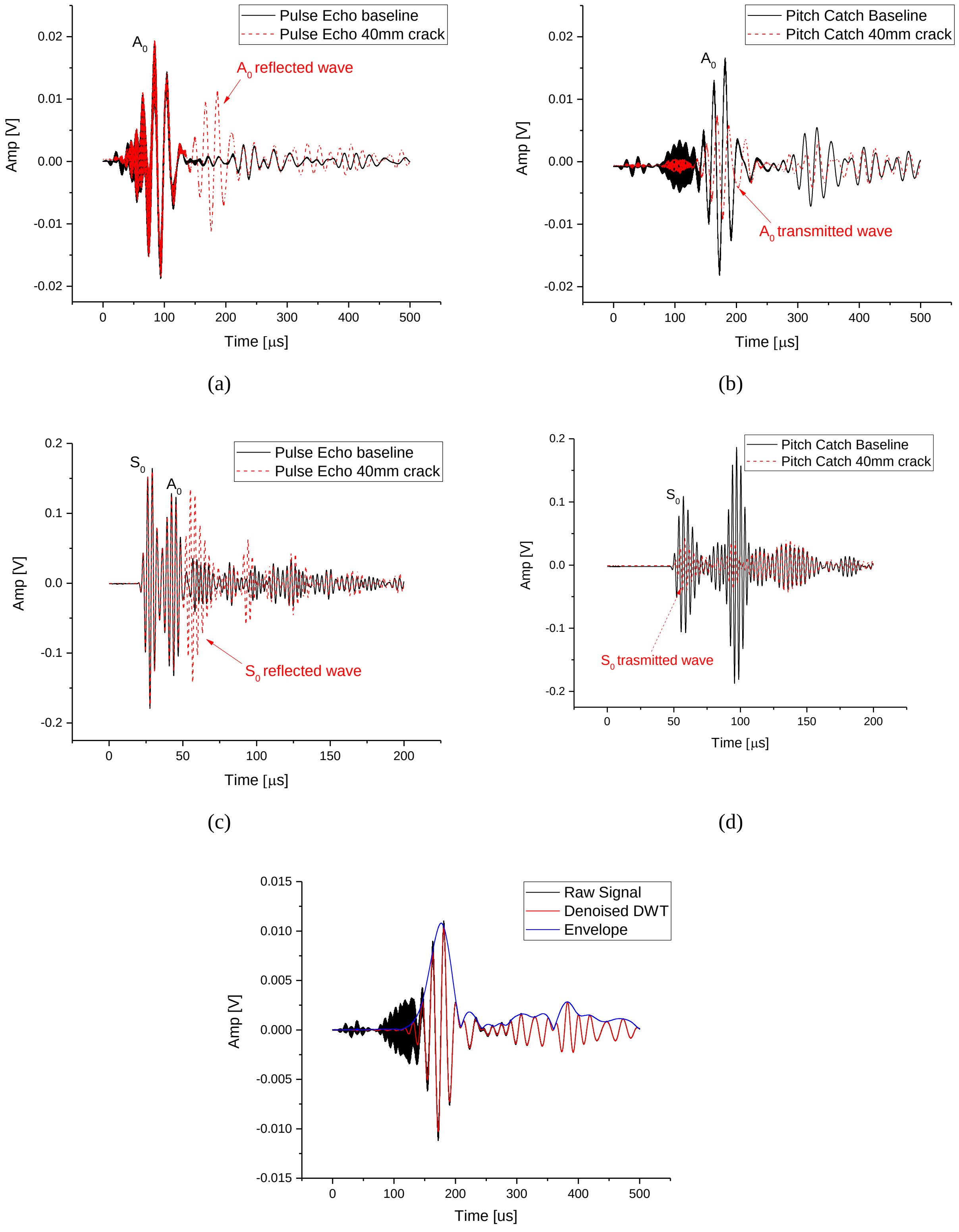

(a) (b)

(c) (d)

(e)

Figure 5

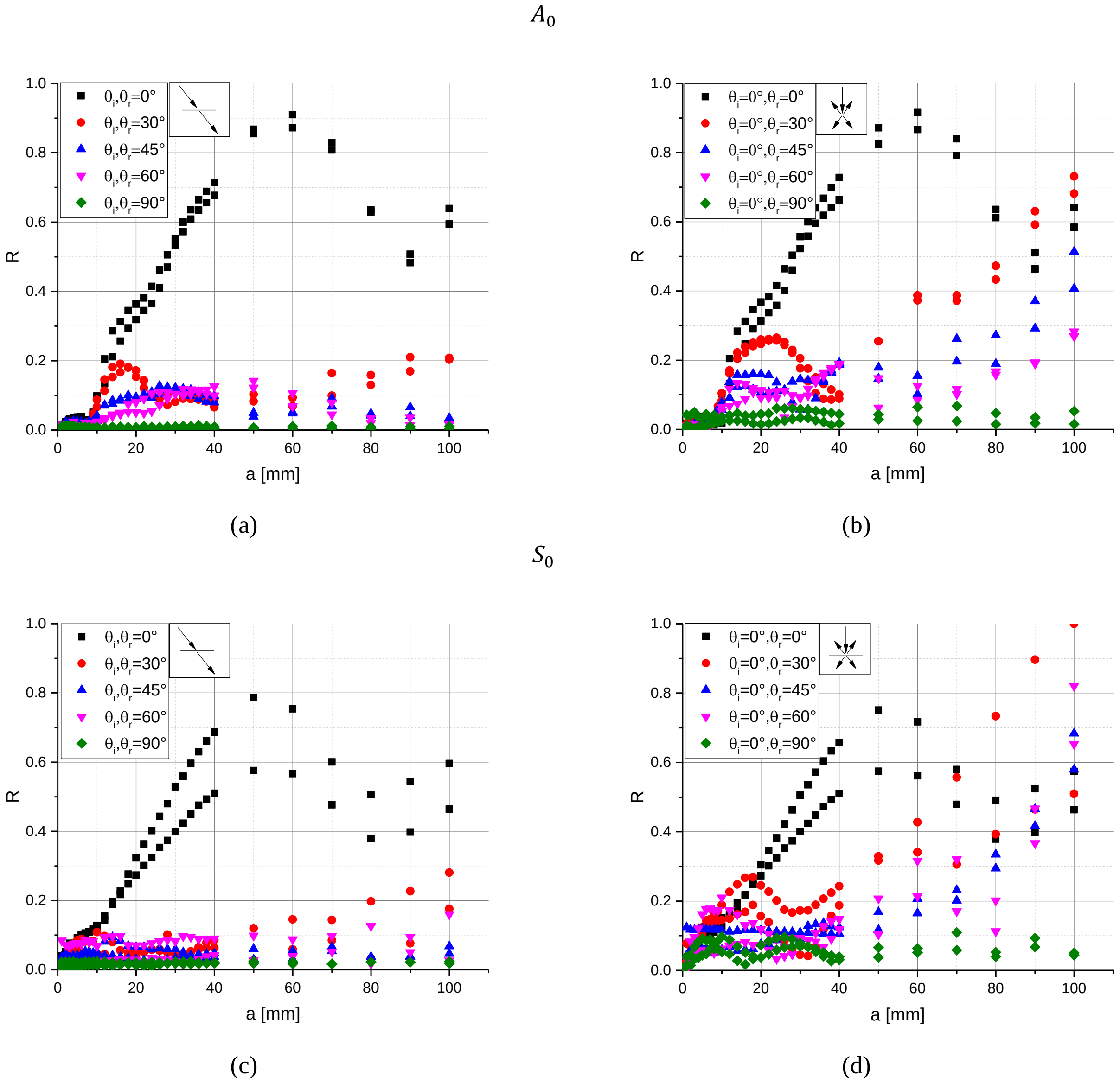

(a) (b) (c) (d)

Figure 6

A_0

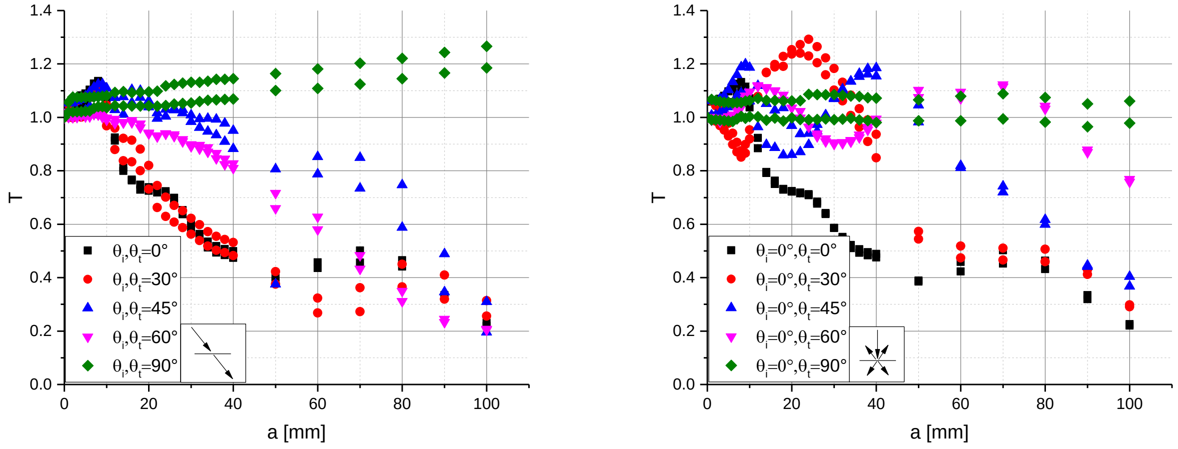

(a) (b)

S_0

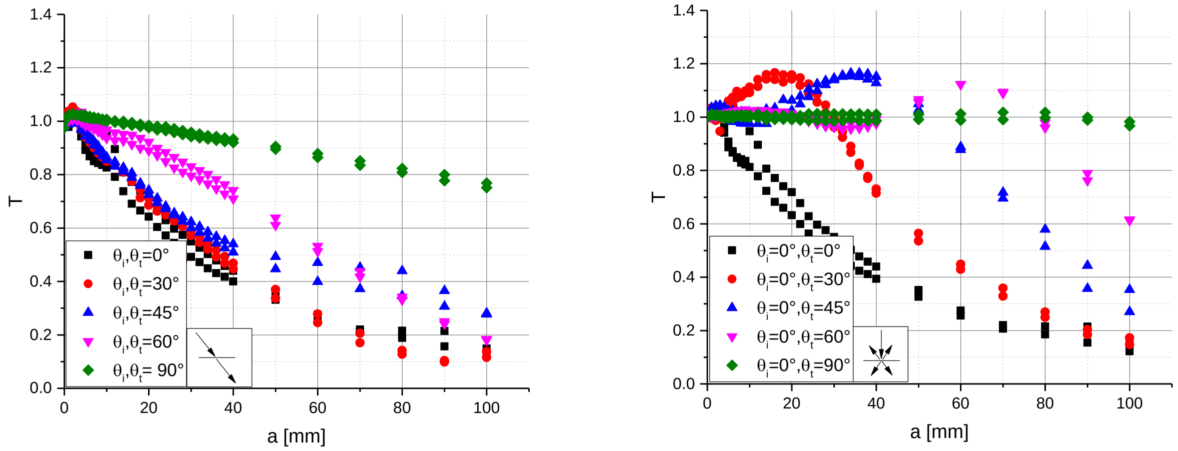

(c) (d)

Figure 7

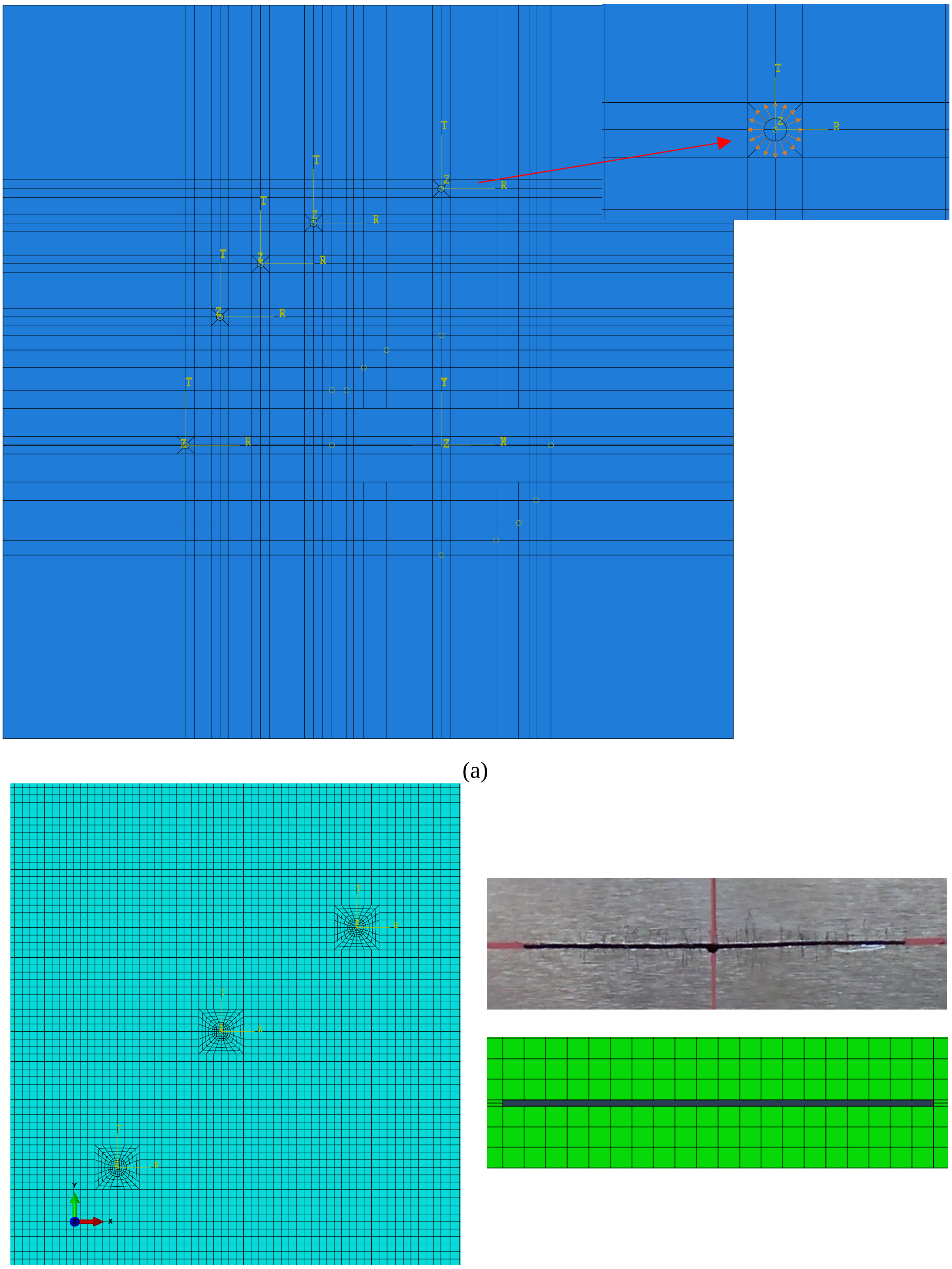

(a)

(b)

(c)

Figure 8

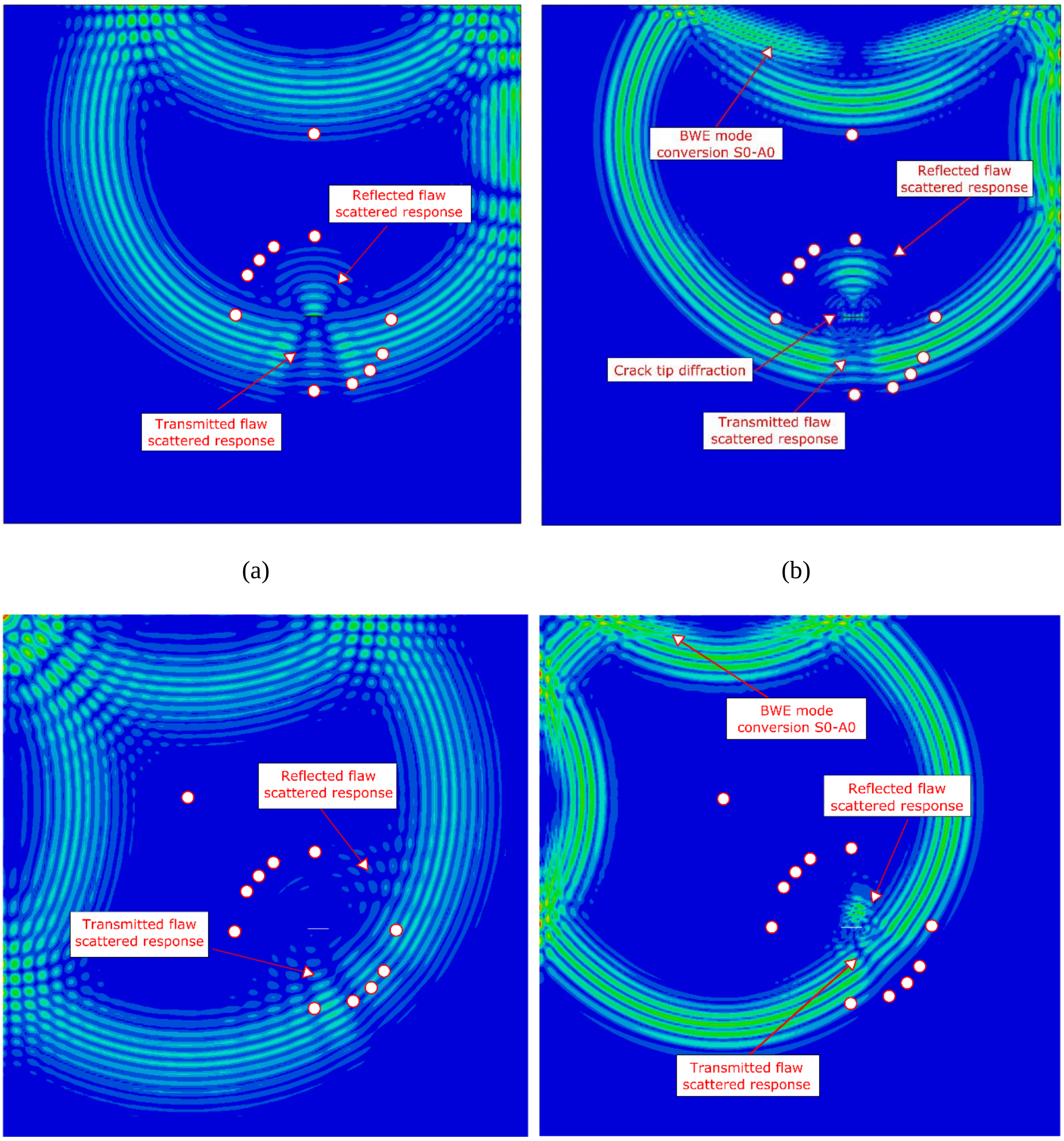

(a) (b)

(c) (d)

Figure 9

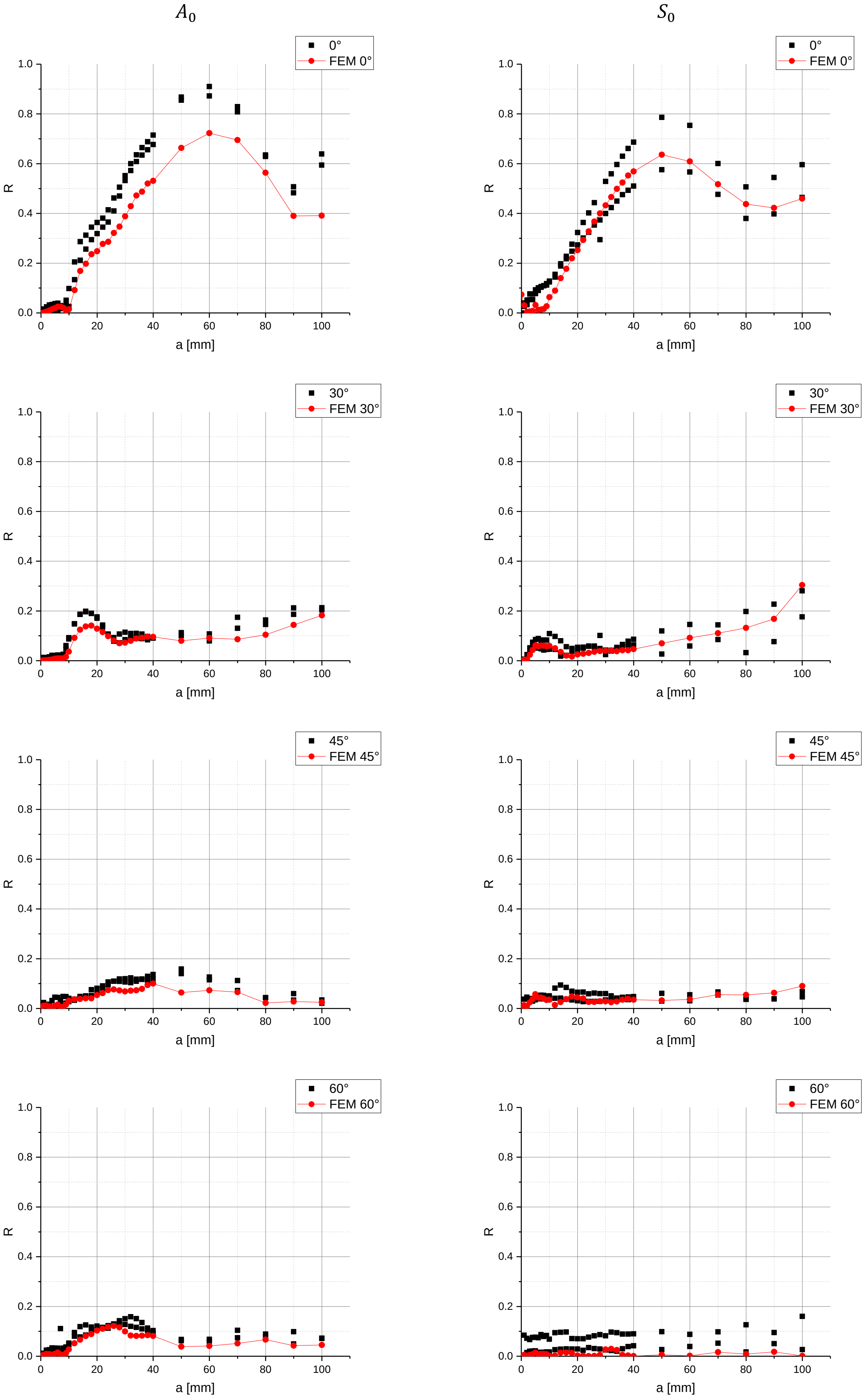
A_0
S_0
0°
FEM 0°
30°
FEM 30°
45°
FEM 45°
60°
FEM 60°
R
0.0
0.2
0.4
0.6
0.8
1.0
a [mm]
0
20
40
60
80
100

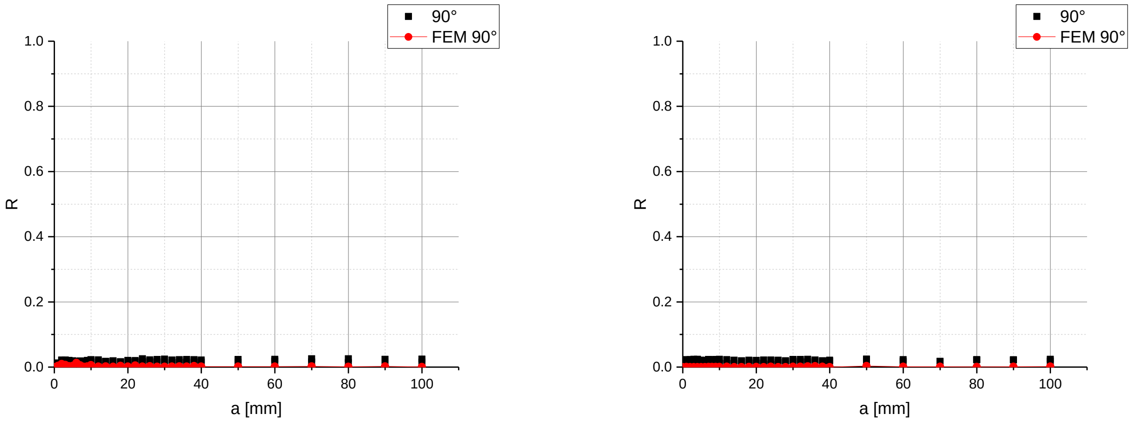

(a)

(b)

Figure 10

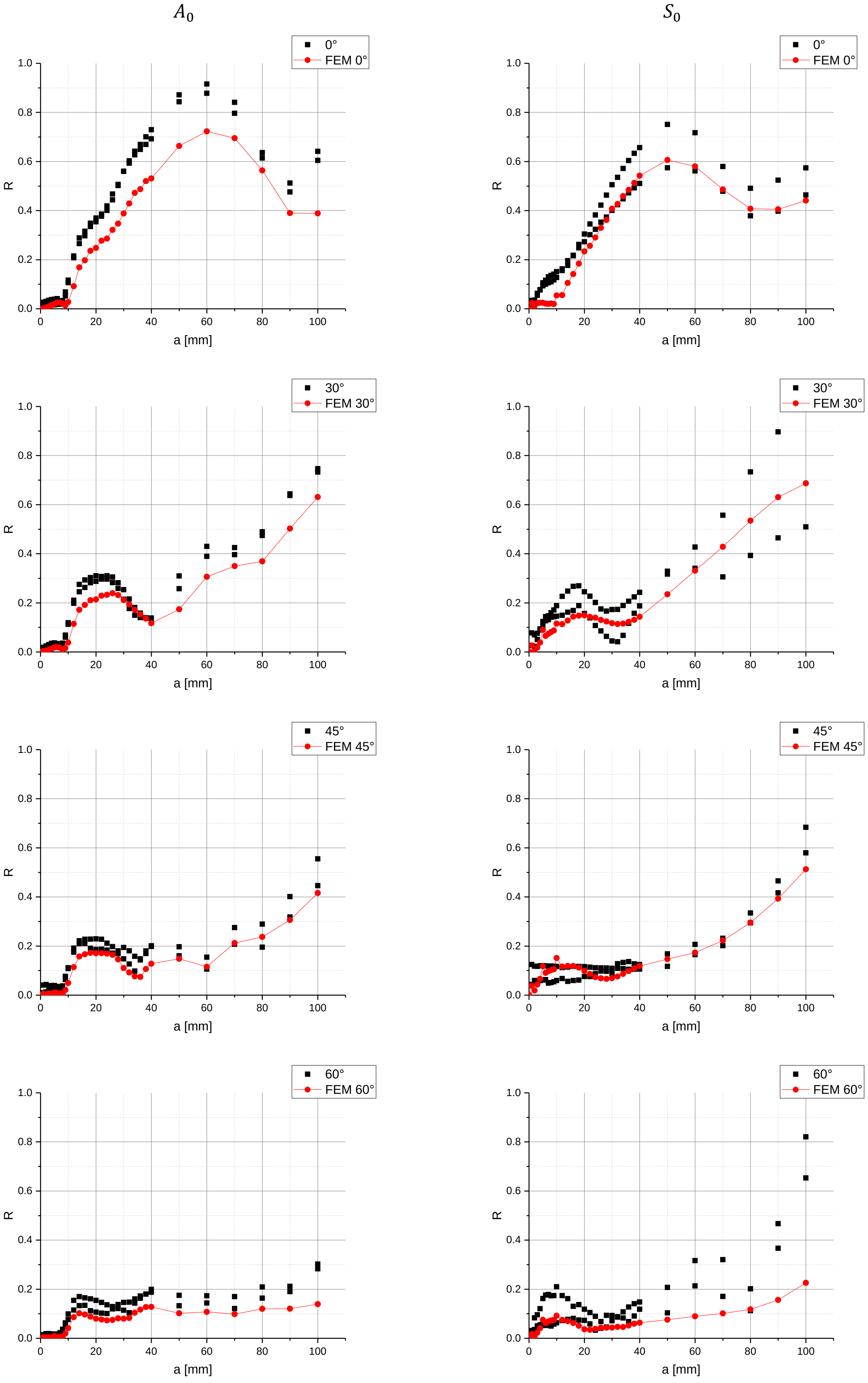
A_0
S_0
0°
FEM 0°
30°
FEM 30°
45°
FEM 45°
60°
FEM 60°
R
a [mm]
0.0
0.2
0.4
0.6
0.8
1.0
0
20
40
60
80
100

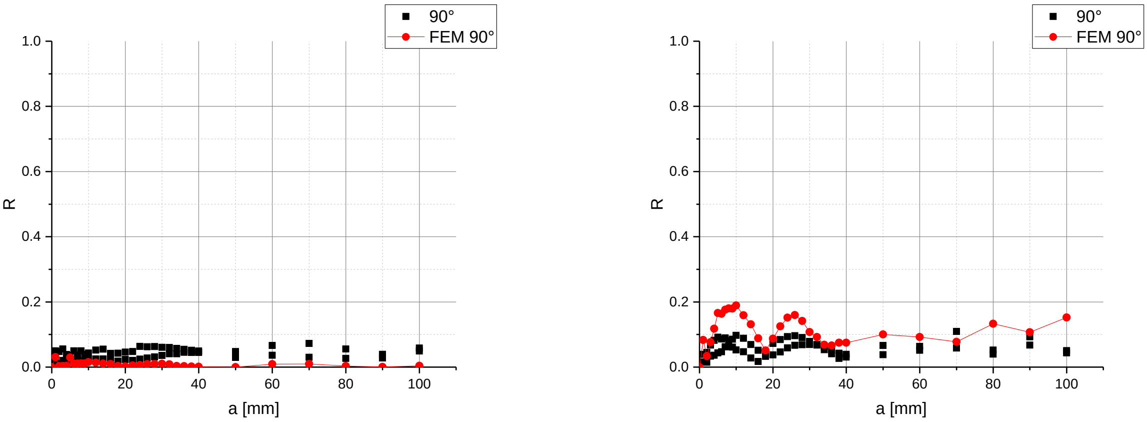
90°
FEM 90°
R
1.0
0.8
0.6
0.4
0.2
0.0
0
20
40
60
80
100
a [mm]
90°
FEM 90°
R
1.0
0.8
0.6
0.4
0.2
0.0
0
20
40
60
80
100
a [mm]

(a) (b)

Figure 11

A_0

S_0

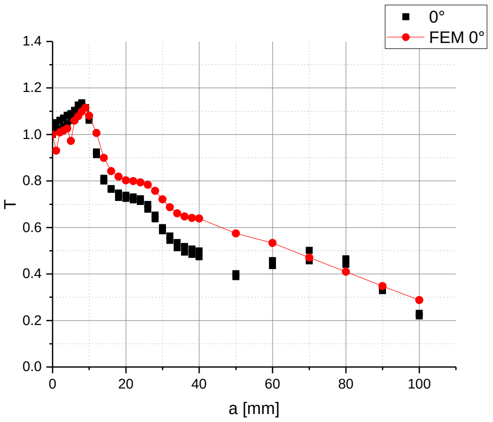

0°
FEM 0°
T
1.4
1.2
1.0
0.8
0.6
0.4
0.2
0.0
0
20
40
60
80
100
a [mm]

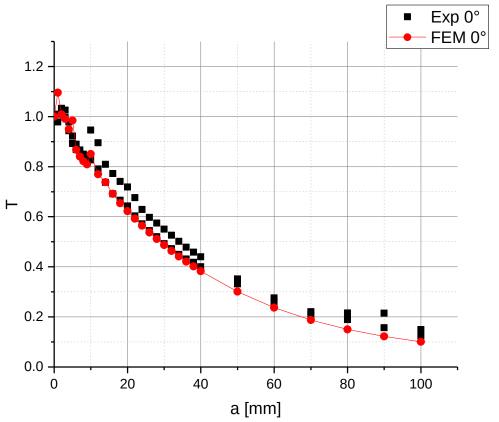

Exp 0°
FEM 0°
T
1.2
1.0
0.8
0.6
0.4
0.2
0.0
0
20
40
60
80
100
a [mm]

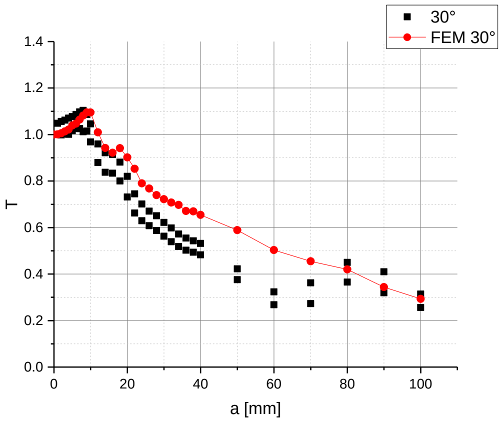

30°
FEM 30°
T
1.4
1.2
1.0
0.8
0.6
0.4
0.2
0.0
0
20
40
60
80
100
a [mm]

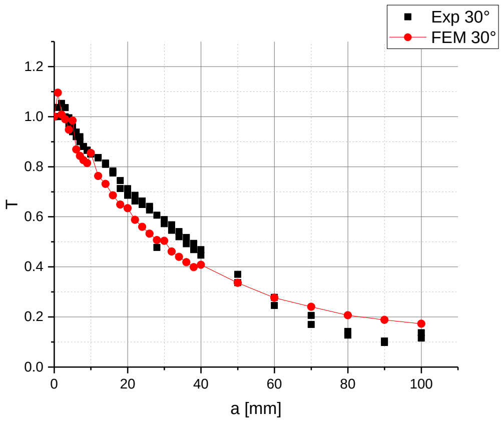

Exp 30°
FEM 30°
T
1.2
1.0
0.8
0.6
0.4
0.2
0.0
0
20
40
60
80
100
a [mm]

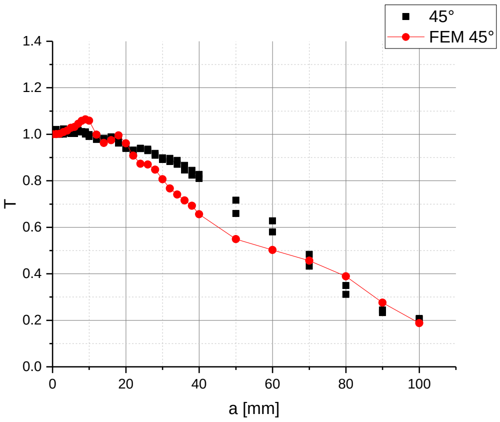

45°
FEM 45°
T
1.4
1.2
1.0
0.8
0.6
0.4
0.2
0.0
0
20
40
60
80
100
a [mm]

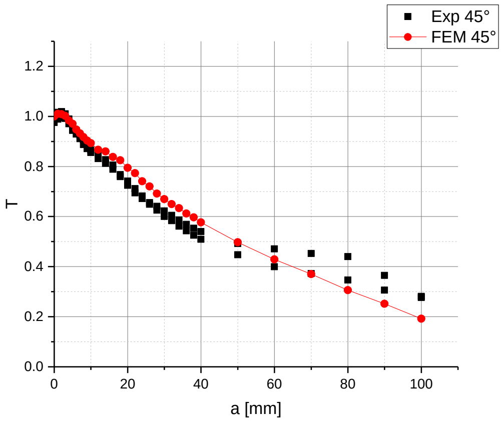

Exp 45°
FEM 45°
T
1.2
1.0
0.8
0.6
0.4
0.2
0.0
0
20
40
60
80
100
a [mm]

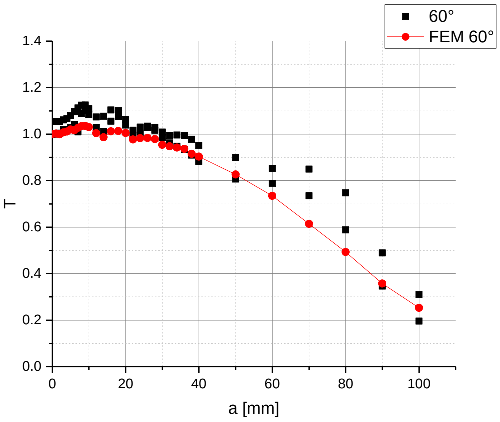

60°
FEM 60°
T
1.4
1.2
1.0
0.8
0.6
0.4
0.2
0.0
0
20
40
60
80
100
a [mm]

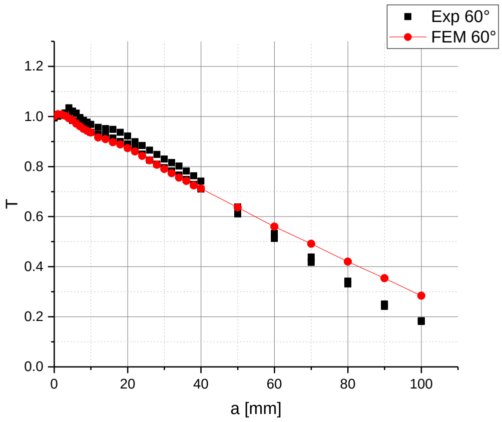

Exp 60°
FEM 60°
T
1.2
1.0
0.8
0.6
0.4
0.2
0.0
0
20
40
60
80
100
a [mm]

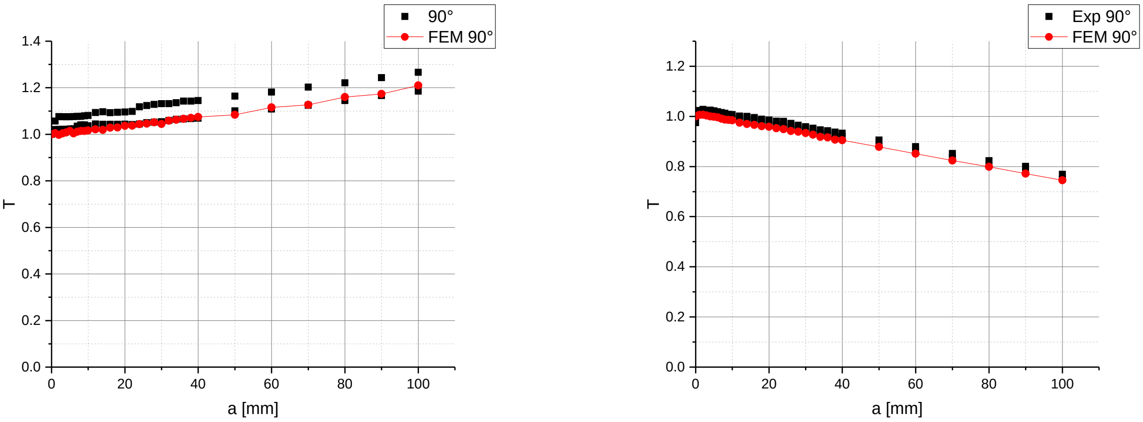
90°
FEM 90°
1.4
1.2
1.0
0.8
0.6
0.4
0.2
0.0
T
0
20
40
60
80
100
a [mm]
Exp 90°
FEM 90°
1.2
1.0
0.8
0.6
0.4
0.2
0.0
T
0
20
40
60
80
100
a [mm]

(a) (b)

Figure 12

A_0

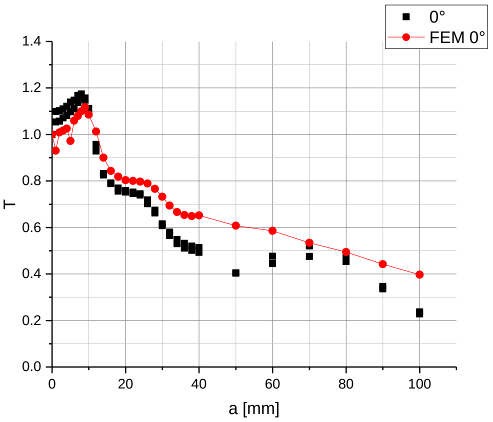
0°
FEM 0°
T
a [mm]
0.0 0.2 0.4 0.6 0.8 1.0 1.2 1.4
0 20 40 60 80 100

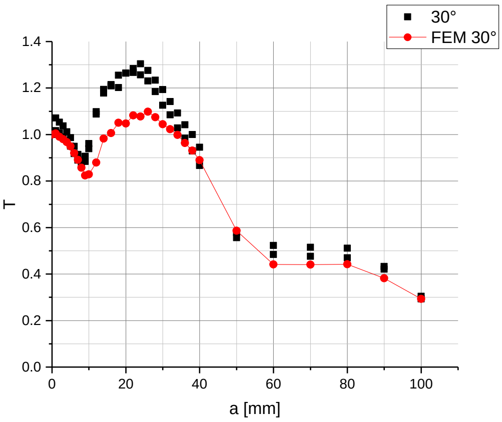
30°
FEM 30°
T
a [mm]
0.0 0.2 0.4 0.6 0.8 1.0 1.2 1.4
0 20 40 60 80 100

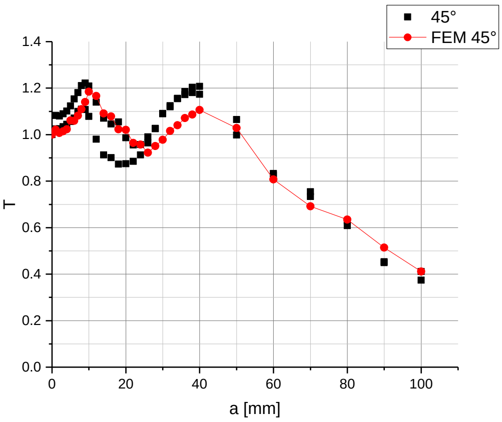
45°
FEM 45°
T
a [mm]
0.0 0.2 0.4 0.6 0.8 1.0 1.2 1.4
0 20 40 60 80 100

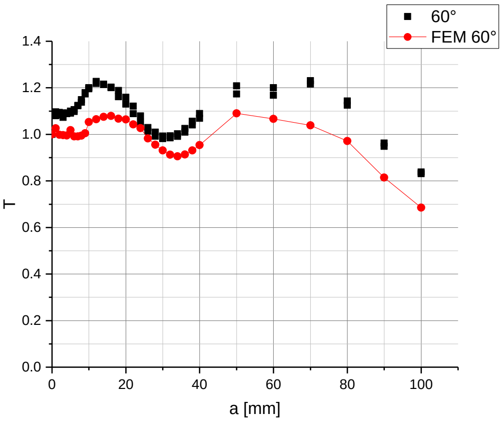
60°
FEM 60°
T
a [mm]
0.0 0.2 0.4 0.6 0.8 1.0 1.2 1.4
0 20 40 60 80 100

S_0

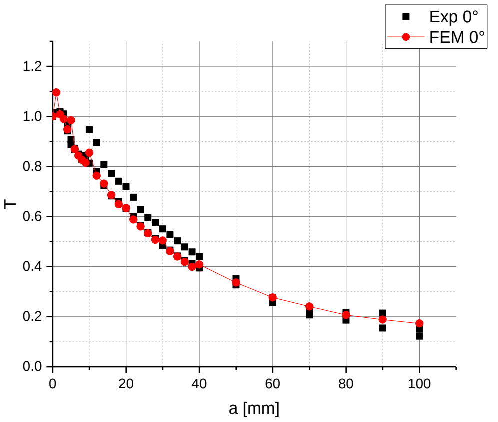
Exp 0°
FEM 0°
T
a [mm]
0.0 0.2 0.4 0.6 0.8 1.0 1.2
0 20 40 60 80 100

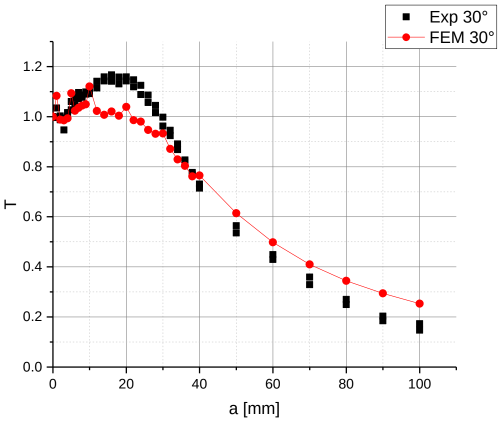
Exp 30°
FEM 30°
T
a [mm]
0.0 0.2 0.4 0.6 0.8 1.0 1.2
0 20 40 60 80 100

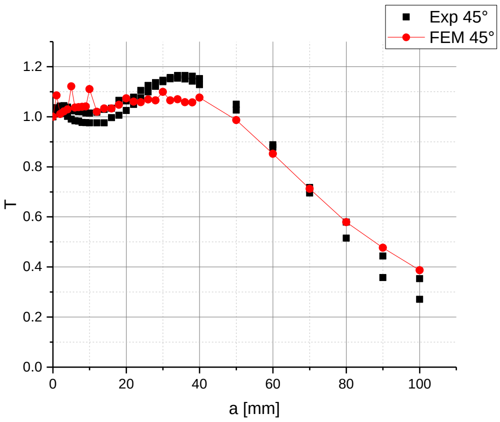
Exp 45°
FEM 45°
T
a [mm]
0.0 0.2 0.4 0.6 0.8 1.0 1.2
0 20 40 60 80 100

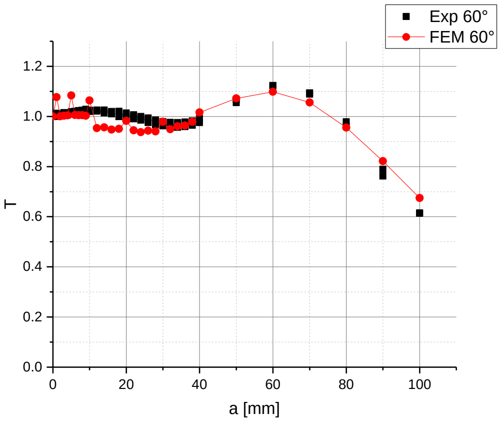
Exp 60°
FEM 60°
T
a [mm]
0.0 0.2 0.4 0.6 0.8 1.0 1.2
0 20 40 60 80 100

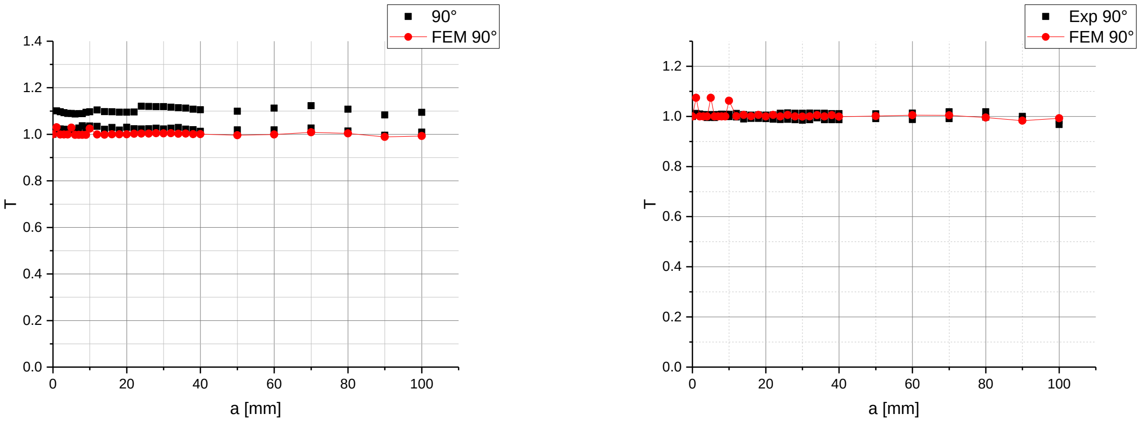
■ 90°
● FEM 90°
T
1.4
1.2
1.0
0.8
0.6
0.4
0.2
0.0
0
20
40
60
80
100
a [mm]
■ Exp 90°
● FEM 90°
T
1.2
1.0
0.8
0.6
0.4
0.2
0.0
0
20
40
60
80
100
a [mm]

(a) (b)

Figure 13

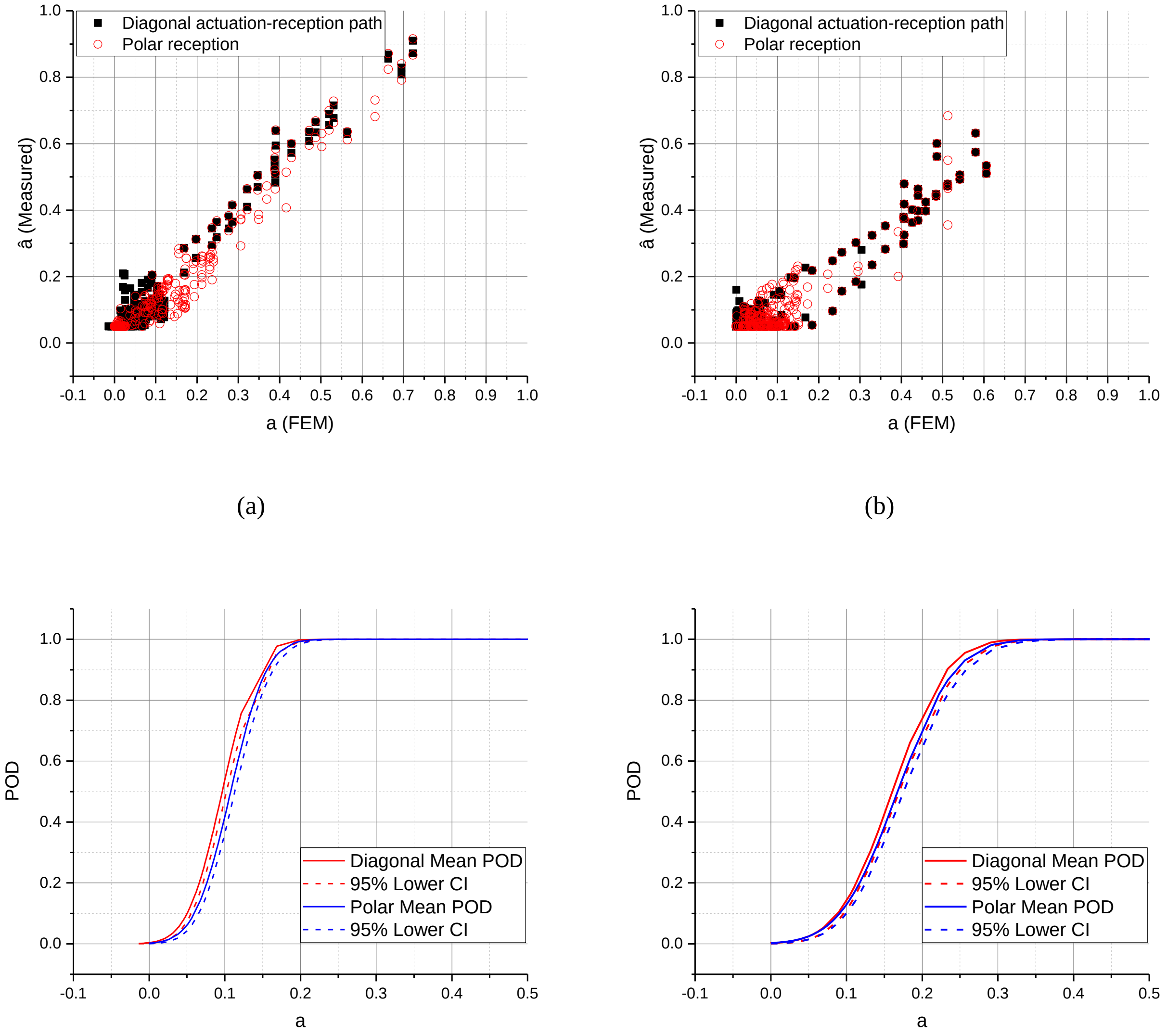

(a) (b)

(c) (d)

Figure 14

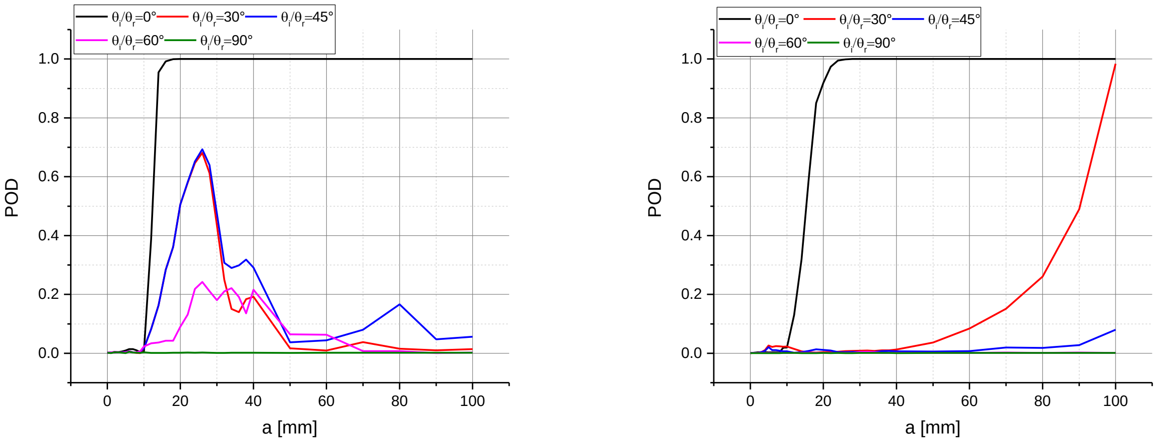
θi/θr=0°
θi/θr=30°
θi/θr=45°
θi/θr=60°
θi/θr=90°
POD
0.0
0.2
0.4
0.6
0.8
1.0
0
20
40
60
80
100
a [mm]

(a) (b)

Figure 15

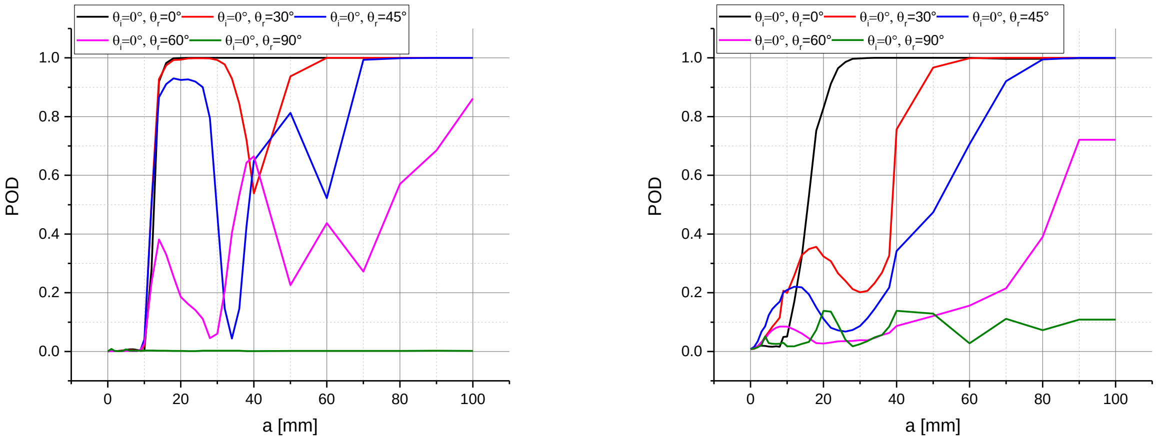
θi=0°, θr=0°
θi=0°, θr=30°
θi=0°, θr=45°
θi=0°, θr=60°
θi=0°, θr=90°
POD
1.0
0.8
0.6
0.4
0.2
0.0
0
20
40
60
80
100
a [mm]
θi=0°, θr=0°
θi=0°, θr=30°
θi=0°, θr=45°
θi=0°, θr=60°
θi=0°, θr=90°
POD
1.0
0.8
0.6
0.4
0.2
0.0
0
20
40
60
80
100
a [mm]

(a) (b)

Figure 16

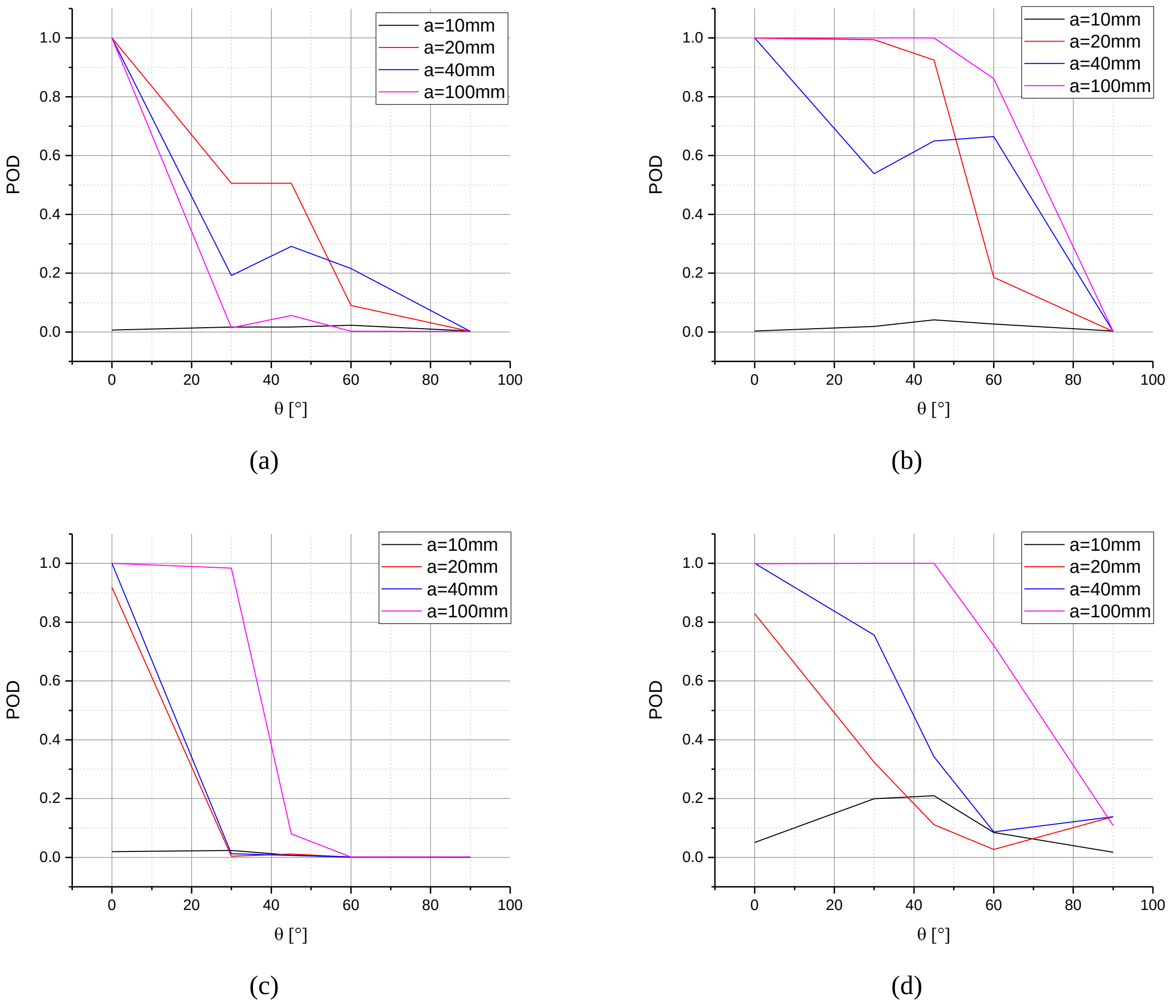

(a)

(b)

(c)

(d)

Figure 17